A tonically active master neuron continuously modulates mutually exclusive motor states at two-time scales

Jun Meng[1,2], Tosif Ahamed[2]*, Bin Yu[3], Wesley Hung[2], Sonia El Mouridi[4,5], Zezhen Wang[6], Yongning Zhang[3], Quan Wen[6], Thomas Boulin[4], Shangbang Gao[3]*, Mei Zhen[1,2,7]*

1. Department of Physiology, University of Toronto, Toronto, ON, Canada
2. Lunenfeld-Tanenbaum Research Institute, Mount Sinai Hospital, Toronto, ON, Canada
3. Huazhong University of Science and Technology, Wuhan, China
4. Univ Lyon, Université Claude Bernard Lyon 1, MeLiS, CNRS UMR 5284, INSERM U1314, Institut NeuroMyoGène, Lyon 69008, France
5. Current address: King Abdullah University of Science and Technology (KAUST), Biological and Environmental Science and Engineering Division (BESE), KAUST Environmental Epigenetics Program (KEEP), Thuwal, 23955-6900, Saudi Arabia
6. Division of Life Sciences and Medicine, University of Science and Technology of China, Hefei, Anhui, China
7. Lead contact

* Correspondence

Highlights

- Mutually exclusive forward and backward motor states are inherently asymmetric
- Forward and backward motor states are not separately controlled
- A master neuron underlies continuous modulation and transitions of opposing states
- A tonically active premotor interneuron functions as the master neuron

Abstract

Continuity of behaviors requires animals to make smooth transitions between successive and mutually exclusive behavioral states. Neural principles that govern these transitions are not well understood. *C. elegans* spontaneously switch between two opposite motor states, forward and backward movement, a phenomenon long thought to reflect the reciprocal inhibition between two interneurons that separately gate the forward and backward motor circuits, AVB and AVA. Combining experimental data and mathematical modeling, we report that spontaneous forward and backward locomotion and their corresponding motor circuits are not separately controlled. AVA and AVB are neither functionally equivalent nor strictly reciprocally inhibitory. Instead, while AVA phasically inhibits the forward promoting interneuron AVB at a fast timescale, it maintains a tonic, extrasynaptic excitation on AVB over the longer timescale. AVA's depolarized spontaneous membrane potential is necessary for this tonic excitation. We propose a new, master neuron model for locomotion. AVA, with tonic and phasic activity of opposite polarities on different time scales, acts as a master neuron to break the symmetry between the underlying forward and backward motor circuits. This offers a parsimonious solution for sustained locomotion consisted of mutually exclusive motor states.

Introduction

Animal behaviors are displayed as a sequence of discrete, often mutually-exclusive motor states[1–11] such as forward and backward locomotion. Prevailing models for selecting and switching between mutually-exclusive circuit activity patterns include the winner-take-all and reciprocal inhibitory networks[12–16]. However, at shorter timescales, gradual transitions observed between successive motor states may also require continuous, albeit rapid modulation of dynamical variables. For example, locomotion velocity undergoes a continuous change in magnitude, not just a sudden change in sign, when switching between forward and backward movement[3,17–20]. The vertebrate limb movement is correlated with rotational, instead of alternating spinal neural network activity dynamics[21]. However, circuit solutions for continuous modulation that underlie smooth behavioral state transitions are not well understood.

C. elegans exhibits two mutually exclusive motor states: forward movement and backward movement, propelled by the posteriorly and anteriorly propagating undulatory bending waves, respectively[22]. In isotropic environments, they spontaneously switch between the forward and backward motor states[22]. The long-standing model for selecting and switching between these motor states involves a reciprocally inhibitory circuit motif between two separate modules[6] (Fig. 1A).

Anatomically, two groups of non-spiking premotor interneurons, AVB and AVA, make dominant synaptic inputs onto two groups of motor neurons that separately execute the forward and backward movements (Fig. 1A)[23–26]. Based on these connectivity patterns, it has been assumed that AVA and AVB also independently control backward and forward movement[27–32]. Synaptic connectivity between these modules (Fig. 1A) is thought to regulate transitions and dwell times in each behavioral state[6]. This model explicitly treats the forward and backward states as binary outcomes of two symmetrically wired and functionally independent circuits. Transitions between forward and backward states occur stochastically or are driven by external input[6].

However, previous measurements of *C. elegans* locomotion have revealed features not easily captured by the model of reciprocal inhibition. Examples include the continuous decay of forward speed prior to the transition into backward movement[18,22,33], the period of post-stimulus arousal during which animals exhibit a higher forward velocity after an escape response[34,35], and the observation that reducing the activity of premotor interneurons of the backward module decreases both backward and forward speed[36].

We sought to resolve the relationship between the forward and backward motor circuits during spontaneous locomotion. We integrated behavior, calcium imaging, and

electrophysiology data for AVA and AVB into a simple dynamical systems model for spontaneous switching between forward and backward motor states.

Interestingly, we found that AVA and AVB are not functionally mirrored, independent controllers for the forward and backward motor states. Additionally, their activities are inconsistent with strict reciprocal inhibition. Instead, our results point to a master-slave configuration, where AVA controls AVB at two timescales with opposite polarities.

Specifically, AVA inhibits AVB at short timescales while exciting it at longer timescales. The former results in transient backward movement, while the latter promotes the forward motor state as a whole and transitions from backward movement to forward movement in particular.

Mechanistically, the slow constitutive excitation of AVB results from the tonic acetylcholine activity of AVA due to its depolarized membrane potential.

AVA has long been viewed to play a limited role in the backward motor state, simply triggering a backward movement[30]. Previously, we found that AVA can both inhibit and promote backward movement[28]. Here, we further reveal that it functions as a master neuron for not only the backward motor states, but also forward motor states and transitions between them.

Our results establish an inherent asymmetry in a motor circuit that underlies spontaneous switches between two mutually exclusive motor states. This new and parsimonious circuit solution for selecting and switching between behavioral states should have broad relevance in understanding decision-making circuits.

Results

Asymmetry in AVA and AVB's membrane excitability

To begin exploring their relationships, we first examined AVA and AVB's membrane potential by in situ electrophysiological recording. AVA and AVB do not fire all-or-none action potentials. Instead, their membrane potentials fluctuate in an analog fashion (Fig. 1B)[6,37–42]. Instead of choosing the lowest value at an arbitrarily estimated steady state as the 'resting' potential, we represent their membrane potentials by the range, as well as the dynamics. The range is shown by cumulative distribution, and the dynamics by the joint probability distribution of the membrane voltage and its time derivative (Fig. 1C, D).

Quantification of our AVA whole-cell patch clamp recording supports the previous conclusion[41–43] that AVA maintains a depolarized potential at multiple stable states. AVA's potential ranged from approximately -30 mV to -10 mV (median -23 mV) (Fig. 1C, D). Its fluctuation exhibits two regimes with small time derivatives, one from -30 mV to -20 mV, and the other from -15 mV to -10 mV (Fig. 1C).

In contrast, our recording of AVB revealed its membrane potential at a more hyperpolarized range, approximately from -75mV to -10mV (median -57mV) (Fig. 1D). AVB also exhibited dynamic changes, often larger than that of AVA, in different stable states, most prominently from -75 mV to -45 mV (Fig. 1C).

The distinct membrane potential characteristics between AVA and AVB raise the possibility of their asymmetric roles in motor control. AVA, but not AVB, is likely tonic active. Even at its baseline, AVA's membrane potential is near the opening threshold of UNC-2[44], a high voltage-gated calcium channel that promotes synaptic vesicular release[45–47].

Endogenous manipulation of AVA's membrane excitability

Each neuron's distinct membrane excitability is regulated by its inward Na^+ and outward K^+ leak conductance (Fig. 2A). Most *C. elegans* neurons exhibit analog membrane activity that is likely fine-tuned by a large family of the K^+ leak channel, K2P (Fig. 2A). To endogenously perturb AVA's membrane potential, we genetically engineered TWK-40 (Fig. 2B), a K2P channel that is more abundantly expressed in three neuron classes, AVA, AVB, and DVA, with AVA expression level the highest (Fig. 2C).

TWK-40 forms a functional K^+ leak channel. Heterologous expression of TWK-40 in the HEK293T cells led to a small increase of their outward leak current (Fig. 2D), similar to a

few mammalian K2P channels[48–50]. A gain-of-function (gf) form, which carries a mutation (L181N) that universally increases K2P channel activity[51,52], led to a large increase in the outward leak current that depends on the intracellular K^+ (Fig. 1D).

We then examined the effect of loss-of-function (lf) and gain-of-function (gf) mutations in the *twk-40* genomic locus (Fig. 2B; Methods). As expected, AVA exhibited a decreased and increased outward leak current in *twk-40(lf)* and *twk-40(gf)* animals, respectively (Fig. 3A, left panel). Consistent with the effect of changing outward K^+ leak, AVA's membrane potential became further depolarized in *twk-40(lf)* mutant (~-25mV to 0mV, median -20mV), and hyperpolarized in *twk-40(gf)* (-40mV to -10mV, median -35mV) (Fig. 3A, right panel; Fig. 3S1). AVA-specific restoration of TWK-40 led to increased outward leak current (Fig. 3A, left panel) and hyperpolarization (Fig. 3A, right panel; Fig 3S1).

These findings establish an experimental paradigm of bi-directional, fine-tuned manipulation of AVA's excitability through its endogenous K^+ leak.

Depolarization of AVA potentiates both backward and forward movements

With cell-type specific manipulation of endogenous TWK-40 activity (Methods; Fig. 3S2), we investigated the physiological consequence of AVA's depolarized membrane potential, in the context of the intact motor circuit and spontaneous locomotion.

In the absence of explicit sensory stimuli, wild-type animals spontaneously switch between forward and backward movements. Depleting TWK-40 from AVA alone produced overall increased motor activity, not only in the backward motor state: more frequent transitions between the backward motor state (Fig. 3S3A), prolonged backward movements (Fig. 3S3A), and increased bending during backward (Fig. 3S3A) but strikingly also in the forward motor state: increased bending during forward movement (Fig. 3B). These motor phenotypes were similar to *twk-40(lf)* genetic mutant animals (Fig 3S3B).

An increase in the animal's overall motor activity upon an increased AVA membrane potential reveals AVA's dual modulation of the forward circuit, in contradiction to the reciprocal inhibition model. Strong support for the strictly reciprocal model was a previous observation that optogenetic depolarization of AVA resulted in instantaneous initiation and sustenance of backward movements(Fig. 3S4A)[53,54]. We reasoned that the current stimulation protocols induce strong and acute depolarization that temporarily locks animals into the backward motor state.

We applied a new stimulation protocol that mimics genetic, fine-tuned, constitute membrane depolarization (Methods), to a strain that expresses an activating opsin (Chrimson) specifically in AVA (Methods). Indeed, constitutive and moderate optogenetic activation of AVA potentiated forward movement (Fig. 3C).

Hyperpolarization of AVA decreases both backward and forward movements

Mirroring our observation with the AVA-specific reduction of K^+ leak, AVA-specific increase of K^+ leak (AVA-TWK-40(gf)) (Methods) exerts an inhibitory effect on both forward motor state (Fig. 3B) and backward motor state (Fig. 3S3A), a behavior similar to that of *twk-40(gf)* mutant animals (Fig. 3S3A, B). Both mutants exhibit drastically reduced overall motility, with the backward motor state exhibiting slightly higher sensitivity: forward movement was drastically reduced (Fig. 3B; Fig. 3S3B) and backward movement was fully abolished (Fig. 3S3A).

These defects could not be explained by a potential developmental effect of hyperpolarization. Indeed, when applying an inhibitory opsin (GtACR)-induced, AVA-specific acute silencing (Methods), we also observed strong inhibition of both forward movement (Fig. 3D) and backward (Fig. 3S4B) movement.

Together, AVA's depolarized membrane potential sustains the animal's motility, not only during backward but also forward movements.

AVA unidirectionally regulates AVB during spontaneous forward movement

To investigate the circuit mechanism that underlies AVA's potentiation of forward movement, we examined the effect of ablating neurons that have been implicated in potentiating forward locomotion[29,55] (AVB, PVC) or partitioning the forward and backward motor states[56–61], RIM (Fig. 4S1A).

Consistent with previous reports[29,54,62], ablation of AVB significantly reduced forward movement (Fig. 4S1B). More importantly, ablating AVB in AVA-specific TWK-40(lf) mutants significantly reduced their forward movement (Fig. 4S1C).

However, ablation of other neurons - PVC and RIM - both mediate wiring between AVA and AVB (Fig. 4S1A) - did not attenuate the forward movement of either wild-type animals (Movie S1) or *twk-40(lf)* mutants during spontaneous locomotion (Fig. 4S1A; Movie S2). These results reveal an unexpected, likely direct, potentiation from AVA to AVB.

We asked whether this effect was reciprocal. Specifically, whether AVB also potentiates AVA. We examined the effect of AVB inhibition on the backward motor circuit. As

expected, optogenetic silencing of AVB reduced the forward movement in freely moving animals (Fig. 4A) and decreased AVB's calcium activity in immobilized animals (Fig. 4S2A). In these animals, the backward movement was unchanged (Fig. 4A), and AVA's activity pattern was similar with or without AVB silencing (Fig. 4B).

The lack of a significant effect of AVB silencing on AVA contrasted with the effect of AVA silencing on AVB (Fig. 4D). Consistent with the finding that silencing of AVA led to attenuated forward movement (Fig. 3), AVA-specific optogenetic silencing reduced calcium activity in both AVA (Fig. 4S2B) and AVB (Fig. 4B) in immobilized animals.

Lastly, we directly assessed the effect of AVA perturbation on AVB's membrane potential (Fig. 4C, D). When AVA was further depolarized, AVB exhibited a significant increase in the amplitude of potential changes (Fig. 4C; AVA-TWK-40(lf)) and a more depolarized membrane potential (~-50mV to -10mV, median -32mV) (Fig. 4D). Conversely, when AVA was hyperpolarized, AVB's membrane potential change was drastically reduced (Fig. 4C; AVA-TWK-40(gf)), with a modest hyperpolarization (~-75mV to -30mV, median -58mV) (Fig. 4D).

These experimental findings reveal a more comprehensive relationship between AVA and AVB. Instead of a strict reciprocal inhibition, there is an asymmetry between the forward and backward motor circuits. During spontaneous locomotion, communication is predominantly from AVA to AVB.

A two-timescale model predicts AVA's regulation of AVB

These results raised the need to directly examine the relationship between AVA and AVB neuronal activity, which had not been simultaneously analyzed in freely moving animals[6,28,39]. We performed simultaneous calcium imaging of AVA and AVB during spontaneous locomotion and examined their relationship (Methods).

For both neurons, the largest activity transients occurred during motor state transitions. As reported[28,29,39,63–67], each epoch of AVA transients aligned with a transition event. Specifically, the initiation of a backward movement coincided with the onset of AVA's calcium rise, whereas the exit from a backward movement coincided with the onset of AVA's calcium decay (Fig. 5SA, left panels). During this period, AVB's calcium change was anti-correlated with that of AVA (Fig. 5SB, left panel).

This relationship changed after animals began an exit from the backward movement. While AVA's activity rapidly decayed to a steady baseline, AVB showed a continued rise as the animal exited the backward movement, followed by a slow decay after the animal

entered forward movement (Fig. 5SA, left panels). AVA maintained its baseline calcium signals during subsequent forward movement (Fig. 5SA, left panels).

We sought the simplest mathematical model that describes this dynamic relationship. Because the functional communication between the two neurons was largely unidirectional (Fig. 4; Fig. 4S2), we considered an input/output model where AVA is treated as the input to AVB. The calcium imaging data (Fig. 5A; Fig. 5SA) suggested a model with two timescales: a fast input during backward movements, and a slower one during post-backward movements, to account for two phases of AVB activity dynamics. This led to a simple linear dynamical system model (Fig. 5B).

$$x_{AVB} = a \cdot x_{AVA} + b \cdot y \qquad (1)$$

$$\frac{dy}{dt} = -\frac{1}{\tau} \cdot y + x_{AVA} \qquad (2)$$

where x_{AVB} and x_{AVA} represent the activity of AVB and AVA, respectively; y represents the slow input from AVA (1), given by the leaky-integrator in (2). The model has three free parameters: the strength of the fast input, a, the strength of the slow input, b, and the timescale for the slow input, τ.

We used the framework of linear systems identification to fit parameters to our calcium imaging data (Fig. 5C; Methods). The best-fit parameters set the strength of fast input a to a negative value and the slow input b to a positive value (Fig. 5D, wild-type).

Biologically, this could be interpreted as the forward motor circuit receiving inputs from AVA at two timescales with opposite polarities: a fast inhibitory input and a slow excitatory input. In other words, AVA maintains a constitutive and excitatory input on AVB, in addition to a strong activation-mediated inhibitory input to AVB during transitions. Without the slow excitatory input, the gradual decay of AVB activity after a backward movement cannot be predicted by the one timescale model (Fig. 5B, D, wild-type).

With different parameter values, this two-timescale model could also predict the animal's spontaneous velocity from AVA's activity (Fig. 5E, wild-type), thus capturing the continuous modulation of behavior during state transitions.

Together, these results suggest a new model where AVA functions as a master regulator of spontaneous locomotion by bi-directional regulation of AVB at different timescales. A transient but strong depolarization of AVA leads to phasic inhibition during backward movements, while a persistent but weak depolarization of AVA provides tonic excitation to AVB that promotes forward movement between backward movements.

Depolarized membrane potential is necessary for AVA to function as a master regulator

We asked if this master regulator role requires AVA to maintain its depolarized spontaneous membrane potential. We co-imaged AVA and AVB in freely behaving AVA-specific TWK-40(lf) and AVA-specific TWK-40(gf) mutants, and examined their relationships.

When we further depolarized AVA (AVA-TWK-40(lf)), the time-dependent relationships with AVB and velocity are maintained (Fig. 5SA, middle panels; 5B, AVA-TWK-40(lf)). The two-timescale model predicted AVB's activity (Fig. 5C, D) and velocity (Fig. 5E, AVA-TWK-40(lf)) from AVA's calcium signals. Parameters for both inputs showed a trend of further increase, but with a slightly higher value for the fast input a (Fig. 5D, AVA-TWK-40(lf)). Biologically, this suggests that with further depolarization, AVA maintains and strengthens both fast-inhibitory and slow-excitatory inputs.

In AVA-TWK-40(gf) mutants, the relationship between AVA and AVB activity changed completely such that a model was no longer applicable. Both neurons exhibited drastically reduced calcium signals with little dynamical changes (Fig. 5F; Fig. 5SA, right panels).

These results suggest that the two-time scale model for AVA's master regulator role is contingent on its depolarized membrane potential.

Cholinergic transmission plays a major role in AVA's tonic excitation of the forward motor state

A constitutive input from AVA that requires maintained depolarized membrane potential implicates AVA's tonic activation.

We examined this possibility through dosage-dependent chemogenetic hyperpolarization by a histamine-gated chloride channel (HisCl)[31]. Exposing animals that ectopically express HisCl in AVA led to a histamine-dependent reduction of backward speed, as well as spontaneous forward speed[31]. We further noted that the backward motor circuit exhibited higher sensitivity to histamine. At 2mM, histamine fully blocked the backward movement (Fig. 6A, left panel) but only modestly reduced the forward movement (Fig. 6A, middle panel). With increased histamine, the forward movement progressively declined (Fig. 6A, middle panel).

This result implies that with sequential membrane hyperpolarization, AVA rapidly loses its ability of transient activation that underlies phasic inhibitory input onto the forward

circuit, but gradually loses its constitutive activation that underlies excitatory input onto the forward circuit, thus separating tonic excitation and phasic inhibition of the forward movement. Consistent with AVA's tonic excitation, synaptic vesicle exocytosis from AVA, visualized by SNB-1::pHluorin, remained at 2mM histamine when phasic inhibition was fully blocked (Fig. 6B). Align with this observation, genetic depolarization and hyperpolarization of AVA by *twk-40(lf)* and *twk-40(gf)* genetic mutations led to an increased and decreased SNB-1::pHluorin signal in AVA, respectively (Fig. S61A).

We asked whether AVA's constitutive inputs are mediated by acetylcholine, as AVA functions primarily as a cholinergic neuron but also synthesizes many neuropeptides[68–70]. We use Tetanus toxin (TeTx) to specifically block synaptic vesicle-mediated transmission (Fig. 6S2). AVA-specific expression of TeTx (AVA-TeTx) led to a significant decrease in forward movements, in both wild-type animals (Fig. 6B) and *twk-40(lf)* mutants (Fig. 6S1B). This result was corroborated by the effect of reduced synaptic vesicular loading of acetylcholine, through AVA-specific RNA interference (RNAi)[71] against the acetyltransferase CHA-1[72] (Methods). Similar to AVA-TeTx, but with a slightly milder effect, AVA-specific *cha-1* RNAi led to a reduction of forward movement (Fig. 7C). Lastly, AVA-TeTx fully blocked AVA-mediated, optogenetic potentiation of forward movement (Fig. 6S1C). These results demonstrate that AVA's potentiation of the forward motor circuit requires cholinergic synaptic transmission.

Consistent with its behavioral effect, TeTx disrupted AVA's dynamic relationships with AVB activity (Fig. 6C). In AVA-TeTx animals, AVA continued to exhibit calcium activity transients; however, the correlation between AVA and AVB calcium dynamics was attenuated (Fig. 6D).

We conclude that the tonically active premotor interneuron AVA functions as a master neuron of the *C. elegans* motor circuit. It contributes to both constitutive activation and transient inhibition of the forward motor circuit mainly through cholinergic signaling. Together with previous findings [27,28,60], they lead to an elegant mechanistic model that underlies a spontaneous, continuous motility consisted of dynamic transitions between two mutually opposing motor states (Fig. 7, Discussion).

Discussion

Locomotion is composed of continuous modulation of different behavioral motifs and transitions between them[1–11]. Here we address how a neural system enables this continuous modulation and transition. We summarize below that in *C. elegans*, a tonically active premotor interneuron serves this role, through a bi-directional regulation of two opposing motor states in a master-slave configuration. This new model offers several generalizable biological and evolutionary implications, described after introducing the model.

A master-slave model for continuous motor behaviors

C. elegans intrinsically switches between the forward and backward motor states[22]. Previously, we found that AVA exerts dual modulation of the backward circuit[27,28,60]: at 'rest', AVA reduces spontaneous backward movement through gap junctional-mediated shunting motor neurons that execute backward movement, but initiates backward movement by activating the same group of neurons with chemical synapses when 'activated' (Fig. 7, center panel). Our new finding - AVA's chemical synapse also modulates the forward circuit, with opposite polarities at different time scales (Fig. 7, side panels) - reveals the other side of the same coin: a parsimonious circuit solution for overall motor control.

In this model, AVA is tonically active but switches between a high and low activity state. At its high state, its chemical synapse simultaneously excites the backward circuit and inhibits the forward circuit, which leads to backward movement. As AVA's activity decreases, its chemical synapse's sustained excitation of the forward circuit and its gap junction's sustained inhibition of the backward circuit prevail, leading to the exit of backward movement and transition into the forward movement.

This model makes AVA the master neuron that continuously regulates opposing motor motifs, mediating their intrinsic transitions without losing overall motility.

Asymmetry between the forward and backward motor states

This configuration breaks an assumed functional symmetry between the forward and backward motor circuits.

An inherent asymmetry between the forward and backward functional modules explains several long-noted behavioral characteristics. During spontaneous locomotion, *C. elegans* preferentially sustains forward movement, resulting in a higher propensity of the forward state[22]. But when executed, the shorter backward movement exhibits greater

vigor than the forward movement[73]. Backward movement is more frequently evoked and prolonged when animals encounter repulsive stimuli or attempt to escape[22,73,74]. Importantly, evoked backward movement potently modifies the forward state that follows. A prolonged backward movement is more likely followed by a turn, a form of forward movement that steers away from the original trajectory, whereas a shorter backward movement is more likely followed by forward movement in a similar trajectory[22,75–77], which resembles most spontaneous backward movement. Evoked backward movement further increases the forward speed, potentiating the forward state for up to several minutes[34,35]. Backward movement thus represents an intrinsically more robust, but actively suppressed motor state. Its activation modifies the subsequent forward state.

Anatomic wiring does not account for AVA's full functional connectivity

AVA's function during spontaneous locomotion only partially correlates with its anatomical wiring[23,78,79].

Anatomically, AVA makes extensive chemical and electrical wiring with motor neurons that execute backward movement[23,78,79]. This synaptic connectivity correlates with AVA's regulation of the backward circuit[27,28,32,55,60,80,81].

In contrast, AVA's modulation of the forward circuit cannot be predicted by its anatomical wiring. AVA tonically activates AVB, which contributes to not only sustained forward movement, but also inherently brief backward movement. However, AVA does not have direct synaptic inputs to AVB, whereas AVB makes direct inputs to AVA (Fig. 1A)[23,26,78].

AVA's tonic excitation requires its depolarized membrane potential and cholinergic synaptic transmission. We favor a mechanism in which its depolarized membrane allows constitutive acetylcholine release as a facilitation of extra-synaptic accumulation and potentiation of the forward circuit. Indeed, in the developing larvae, extra-synaptic cholinergic transmission from premotor interneurons provides the tonic potentiation of ventral muscles that functionally substitute for the entire missing ventral subcircuit[82].

Significant inconsistency between functional and anatomical neuronal connectivity has been documented in several systems[83–87]. This implies the necessity of studying other forms of functional communication - ephaptic coupling, extrasynaptic transmission, and modulatory signaling[88–91].

A further, perhaps more interesting intuition from our study is that in a small neural system, with limited numbers of anatomic wiring, the form of 'invisible' wiring might be

preferentially utilized for spontaneous behavioral states, whereas anatomic wiring, such as AVB to AVA, is built mainly for contextual recruitment for decision-making or evoked behaviors.

Essentially, the functional-anatomic connectivity discrepancy might reflect the extend of economical wiring, as the size and cellular complexity of neural systems evolve.

A parsimonious role of the backward motor circuit

Behaviorally, *C. elegans* spends most of its time in the forward state. It is thus intriguing that AVA, the regulator of overall motor control, is the premotor interneuron that is anatomically wired to gate motor neurons that execute the backward movement.

We posit that the motor circuit is built first to generate robust escape responses, which are crucial for survival. The escape circuit is then actively suppressed and repurposed for forward locomotion. In other words, the motor system finds an economical solution by using the same tonic drive to shunt backward and potentiate forward locomotion. Its tonic excitatory input to the forward circuit, an integrated history of its activity, might further serve as the short-term memory of the internal states and environment.

Dynamic regulation of a non-spiking neural network through membrane potential

With a few exceptions[92,93], the *C. elegans* neural system consists primarily of non-spiking neurons[37,42,43,94–98]. This neural network none-the-less generates behaviors that are stable, flexible, and adaptive, as those that function through regenerative potentials.

AVA's functional model suggests that precise and dynamic regulation of the activity of non-spiking neurons and their network can be achieved through the precise modulation of individual membrane potentials. *C. elegans* exceptional expansion of K^+ channels, in particular, the 47 K^+ leak channels[51,99–101] might play an important role.

When a neuron functions through graded potential changes, it is particularly suited for a K2P conductance to regulate its activity range and form of responses to stimuli[99,102]. With 47 K2P genes expressed by overlapping subgroups of 300 neurons[69], these channels could define the unique computational properties of each neuron.

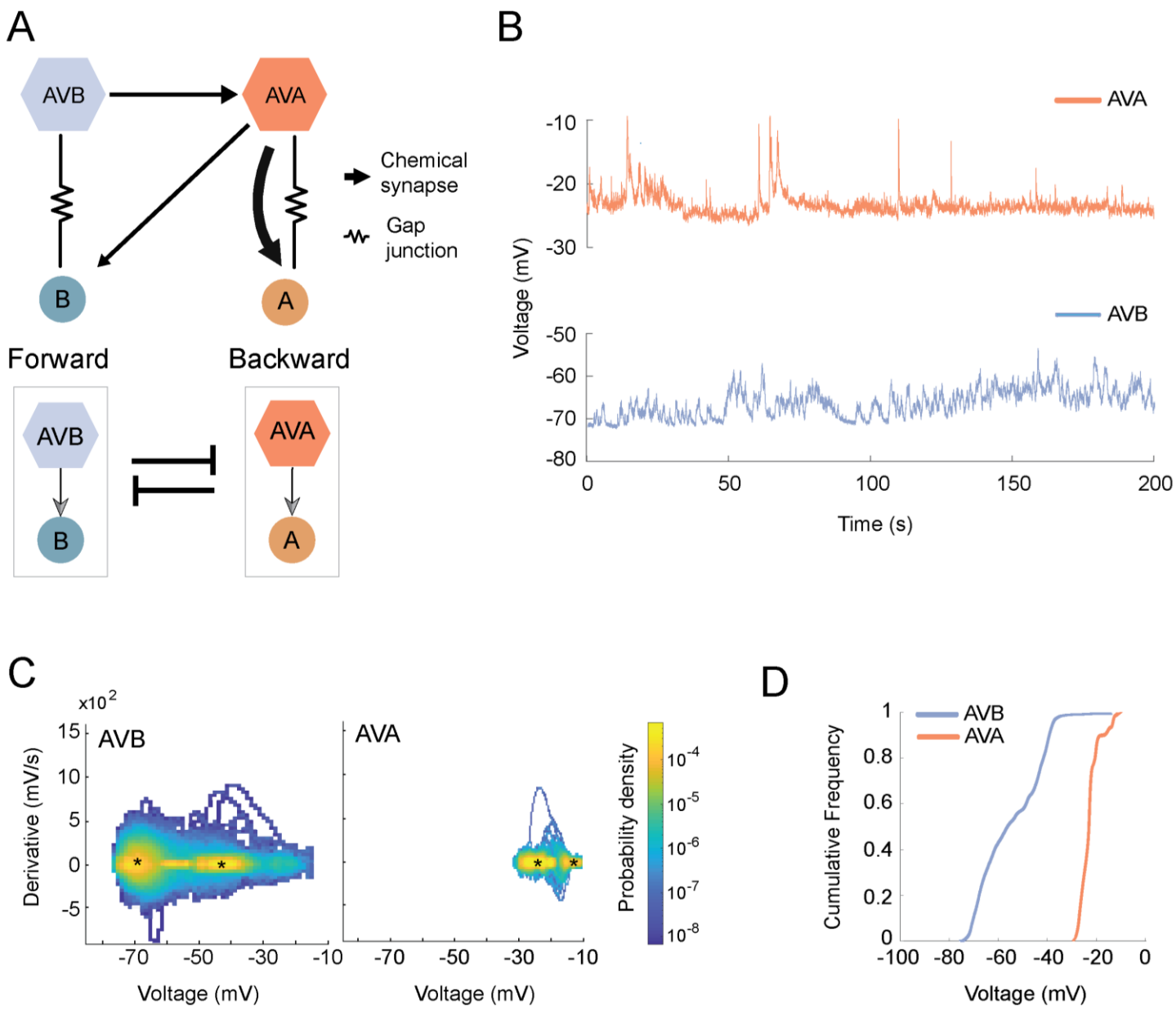
A
AVB
AVA
Chemical synapse
Gap junction
B
A
Forward
Backward
AVB
B
AVA
A
B
AVA
AVB
Voltage (mV)
-10
-20
-30
-50
-60
-70
-80
0
50
100
150
200
Time (s)
C
x10^2
AVB
AVA
Derivative (mV/s)
15
10
5
0
-5
-70
-50
-30
-10
Voltage (mV)
Probability density
10^-4
10^-5
10^-6
10^-7
10^-8
D
AVB
AVA
Cumulative Frequency
1
0.8
0.6
0.4
0.2
0
-100
-80
-60
-40
-20
0
Voltage (mV)

Fig 1

Figure 1. AVA and AVB have distinct membrane potential ranges and dynamics

A. (Upper) Schematics of the adult anatomic wiring diagram for premotor interneurons and motor neurons implicated in directional movement (adapted from[23,78,79]); (Lower) Schematics of previously proposed functional relationship of these neurons[27–31]. **B.** Example traces of spontaneous membrane potential of AVA and AVB neurons by *in situ* whole-cell intracellular recording configuration. **C.** The dynamic range of spontaneous membrane potential for AVB and AVA, is represented by the distribution of spontaneous membrane voltage and its derivatives. * denotes regimes of membrane potentials that might correlate with bi-stability described in previous studies[41–43]. AVB potential drifts over a wider range than AVA (X-axis) and exhibits more frequent but smaller transients than AVA (Y-axis). **D.** Cumulative curves of the distribution of spontaneous membrane potential of AVB and AVA. AVA holds more depolarized membrane potential than AVB. N: 8 and 7 recordings for AVB and AVA, respectively.

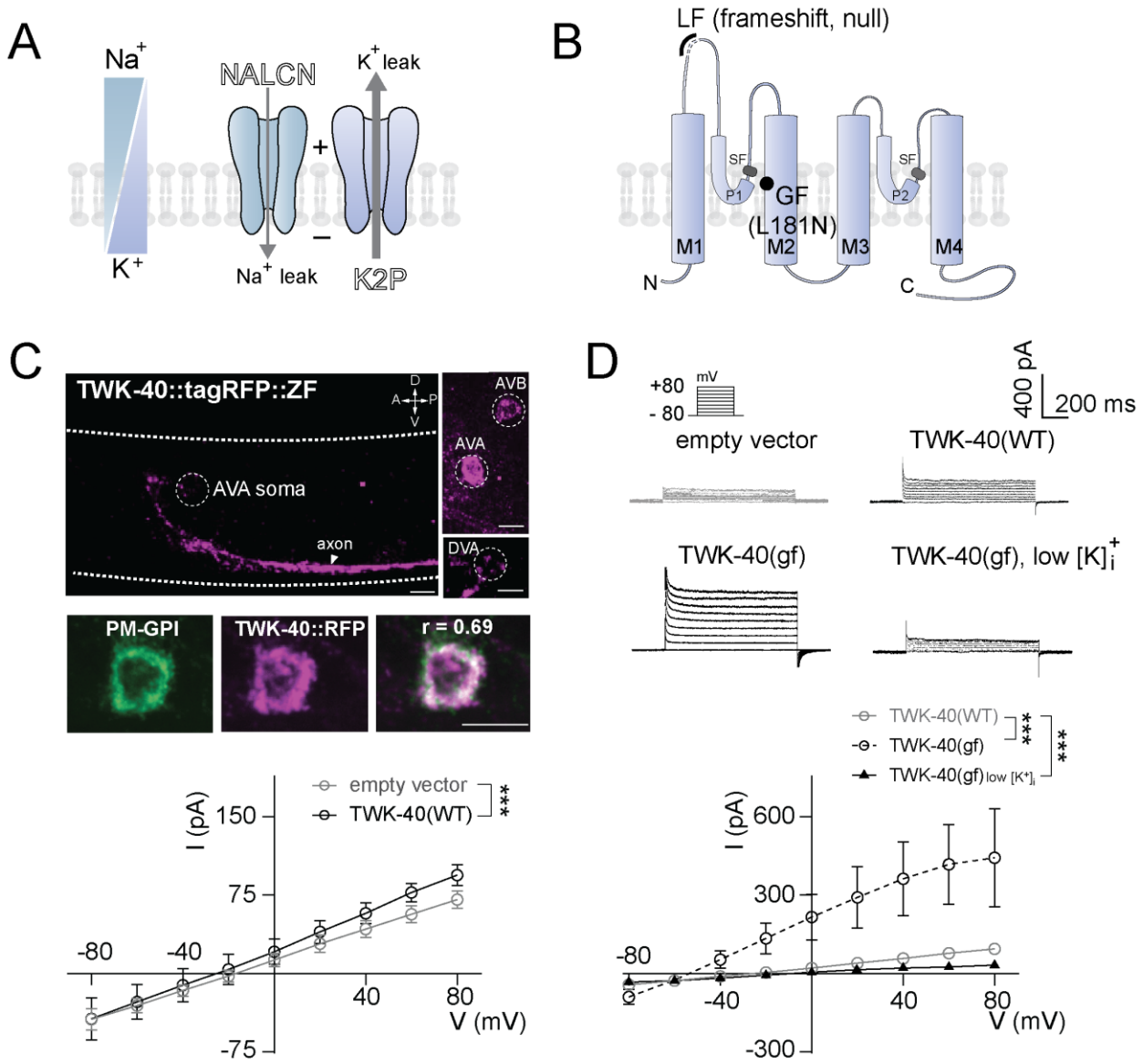
A
Na+
K+
NALCN
K+ leak
+
−
Na+ leak
K2P
B
LF (frameshift, null)
SF
P1
GF
(L181N)
SF
P2
M1
M2
M3
M4
N
C
C
TWK-40::tagRFP::ZF
D
A
P
V
AVB
AVA
AVA soma
axon
DVA
PM-GPI
TWK-40::RFP
r = 0.69
empty vector
TWK-40(WT)
***
I (pA)
150
75
-75
-80
-40
40
80
V (mV)
D
+80
mV
- 80
400 pA
200 ms
empty vector
TWK-40(WT)
TWK-40(gf)
TWK-40(gf), low [K]i+
TWK-40(WT)
TWK-40(gf)
TWK-40(gf) low [K+]i
***
***
I (pA)
600
300
-300
-80
-40
40
80
V (mV)

Fig 2

Figure 2. An endogenous regulator of AVA's spontaneous membrane potential

A. Schematics of the inward sodium and outward potassium leak currents and respective leak channels that contribute to a cell's membrane potential. **B.** Predicted topology of a potassium leak channel (K2P), TWK-40, denoted with genetic mutations that abolish (LF) or increase (GF) potassium leak. M: transmembrane domain; P: pore domain; SF: Selection filter; LF: loss-of-function; null: an allele (*hp834*) with a 7bp deletion that leads to truncation after the M1 domain. GF: Gain-of-function; L181N: an allele (*bln336*) with an activating mutation that promotes the potassium conductance of all K2P channels. **C.** Expression pattern of endogenously tagged TWK-40::tag RFP. (Upper) Confocal images of immunostained TWK-40::TagRFP (anti-TagRFP). Dashed lines outline the animal body; Circles denote somas. The arrowhead labels axonal processes in the ventral nerve cord. Scale bar, 2μm. (Lower) TWK-40::TagRFP (anti-TagRFP) co-localizes with a plasma membrane marker PM-GPI (anti-GFP). r: Pearson's correlation**. D.** (Upper) Representative step currents from HEK293 cells carrying respective heterologous expression vectors by whole-cell voltage-clamp recording. (Lower) I-V curves for respective cells. Quantification showed mean currents and 95% confidence interval (CI) at +80 mV. (Left) cells expressing wild-type TWK-40 (N: 13) showed a small outward current compared to the cell with empty vector (N: 12); (Right) cells expressing TWK-40(GF) showed a large outward current (N: 10), which was diminished by reducing intracellular K^+ concentration (N: 7). *: $P < 0.05$, **: $P < 0.01$, ***: $P < 0.001$ by the Mann-Whitney U tests, with $P < 0.05$ considered to be statistically significant.

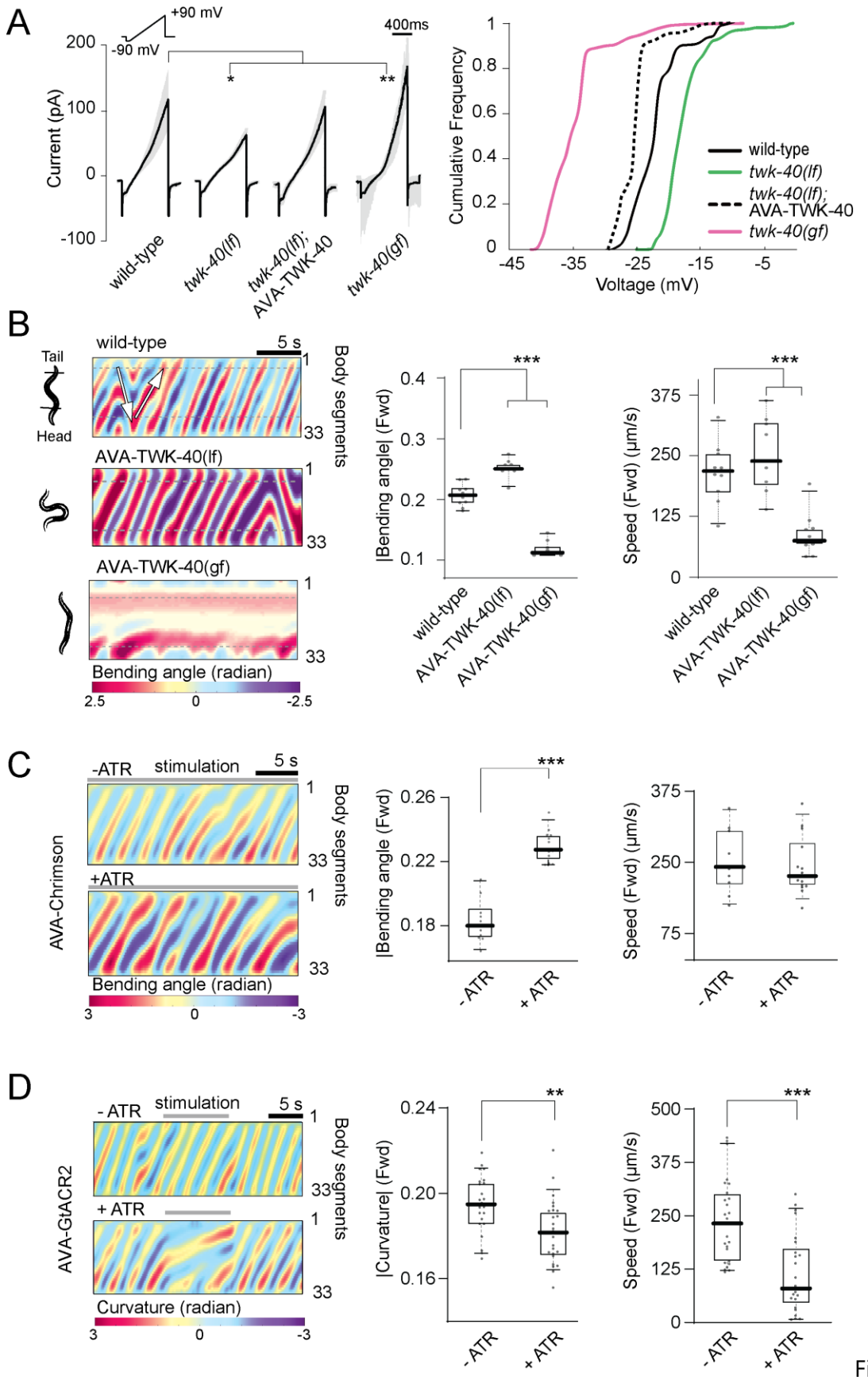
A
+90 mV
-90 mV
400ms
Current (pA)
200
100
0
-100
*
**
wild-type
twk-40(lf)
twk-40(lf); AVA-TWK-40
twk-40(gf)
Cumulative Frequency
Voltage (mV)
-45
-35
-25
-15
-5
B
wild-type
5 s
Tail
Head
Body segments
AVA-TWK-40(lf)
AVA-TWK-40(gf)
Bending angle (radian)
2.5
0
-2.5
|Bending angle| (Fwd)
Speed (Fwd) (µm/s)
***
C
-ATR
stimulation
+ATR
AVA-Chrimson
Bending angle (radian)
3
-3
|Bending angle (Fwd)
D
- ATR
+ ATR
AVA-GtACR2
Curvature (radian)
|Curvature| (Fwd)
**

Fig 3

Figure 3. AVA's depolarized membrane potential maintains forward movement

A. (Left) AVA's leak currents recorded in whole-cell patch clamp configuration with ramping potential from -60mV to +90mV. Black traces and gray areas denote mean currents at +80mV and min/max range, respectively. N: 5 (wild-type), 8 (*twk-40(lf)*), 7 (*twk-40(lf);* AVA-TWK-40), and 7 *twk-40(gf)* cells. (Right) cumulative frequency of AVA's spontaneous potential in respective genotypes. N: 7 (wild-type), 9 (*twk-40(lf)*), 9 (*twk-40(lf);* AVA-TWK-40) and 13 (*twk-40(gf)*) cells. Changing TWK-40's conductance specifically in AVA led to correspondent changes in outward leak currents. **B.** (Left) Representative kymograph of bending angles of a freely moving animal of denoted genotype. Regions between dashed lines denote the animal body. Arrows illustrate directions of bending waves that correspond to either the forward (head to tail), or backward (tail to head) movements. Darker colors denote deeper bending. AVA-specific decrease (LF) or increase (GF) of TWK-40 conductance led to increased or decreased forward movement, respectively. (Right) Quantification of absolute bending angles and centroid speed during forward movement. **C.** (Left) Representative kymographs of freely moving animals with AVA-specific constitutive optogenetic activation (+ATR). Controls (-ATR) were the same animals subjected to the same stimulation protocol but without the supply of the opsin activator. Right, Quantification of bending angles and centroid speed during forward movement. N: 14 (+ATR) and 10 (-ATR) animals. **D.** (Left) Representative kymograph of bending angles of animals subjected to AVA-specific optogenetic inhibition. (Right) Quantification of absolute bending angles and centroid speed during forward movement in non-stimulated (-ATR, N: 28) and stimulated (+ATR, N: 25) animals. Box-whisker plot displays the 90/10 and 75/25 percentiles, respectively. *: $P < 0.05$, **: $P < 0.01$, ***: $P < 0.001$ by the Mann-Whitney U tests. $P < 0.05$ is considered to be statistically significant.

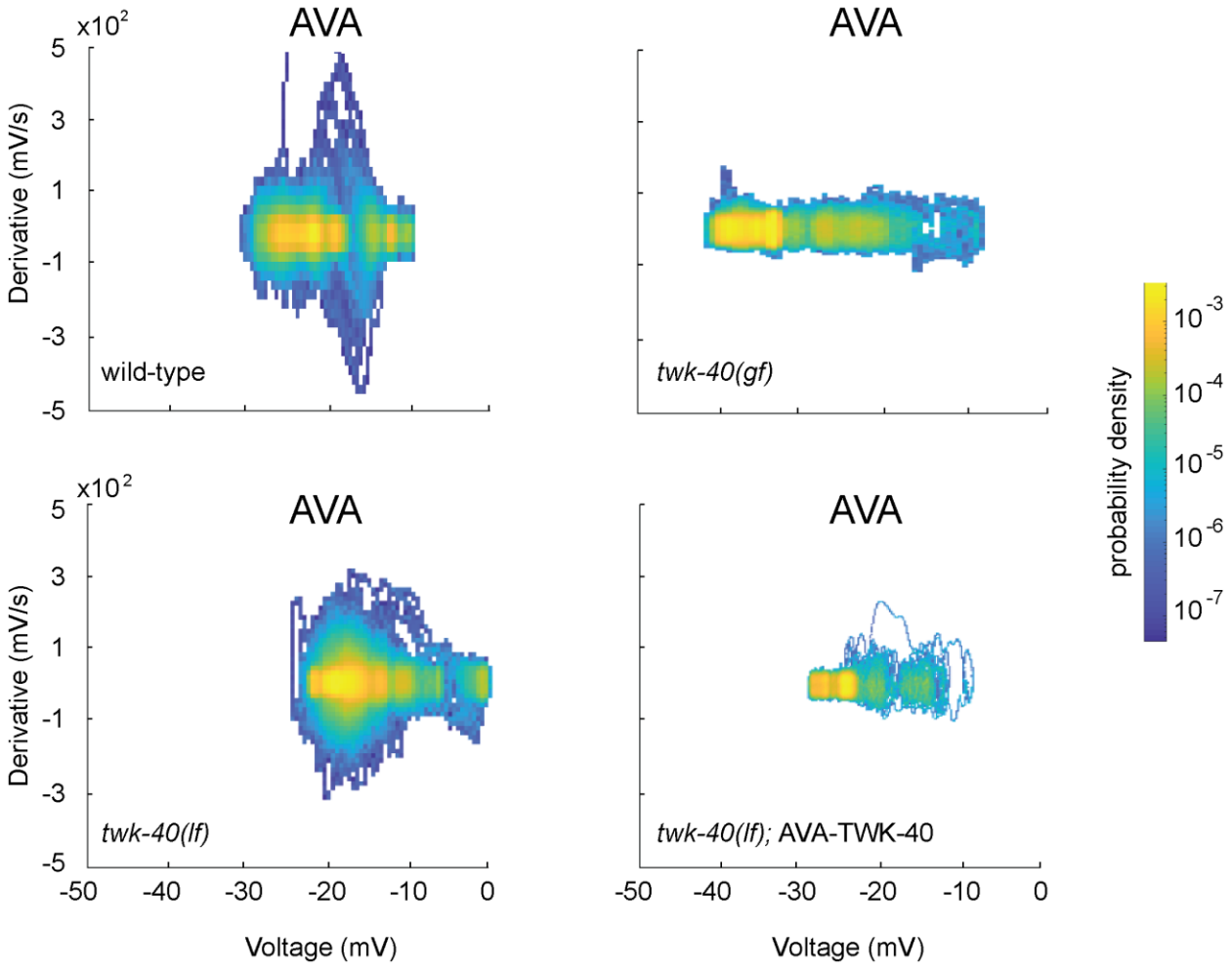

Fig 3S1

Figure 3S1. K^+ leak regulates AVA's membrane and dynamic range

Distribution of the voltage derivatives across AVA's membrane potentials shows an increase and decrease of both the range and dynamic range in *twk-40(lf)* (upper right panel, N:9) and *twk-40(gf)* (lower left panel, N:13) mutant animals, respectively. AVA-specific restoration of wild-type TWK-40 protein in *twk-40(lf)* mutants (lower right panel, N: 8) decreased AVA's range membrane potential and reduced its dynamic range, the latter similar to *twk-40(gf)* mutant animals.

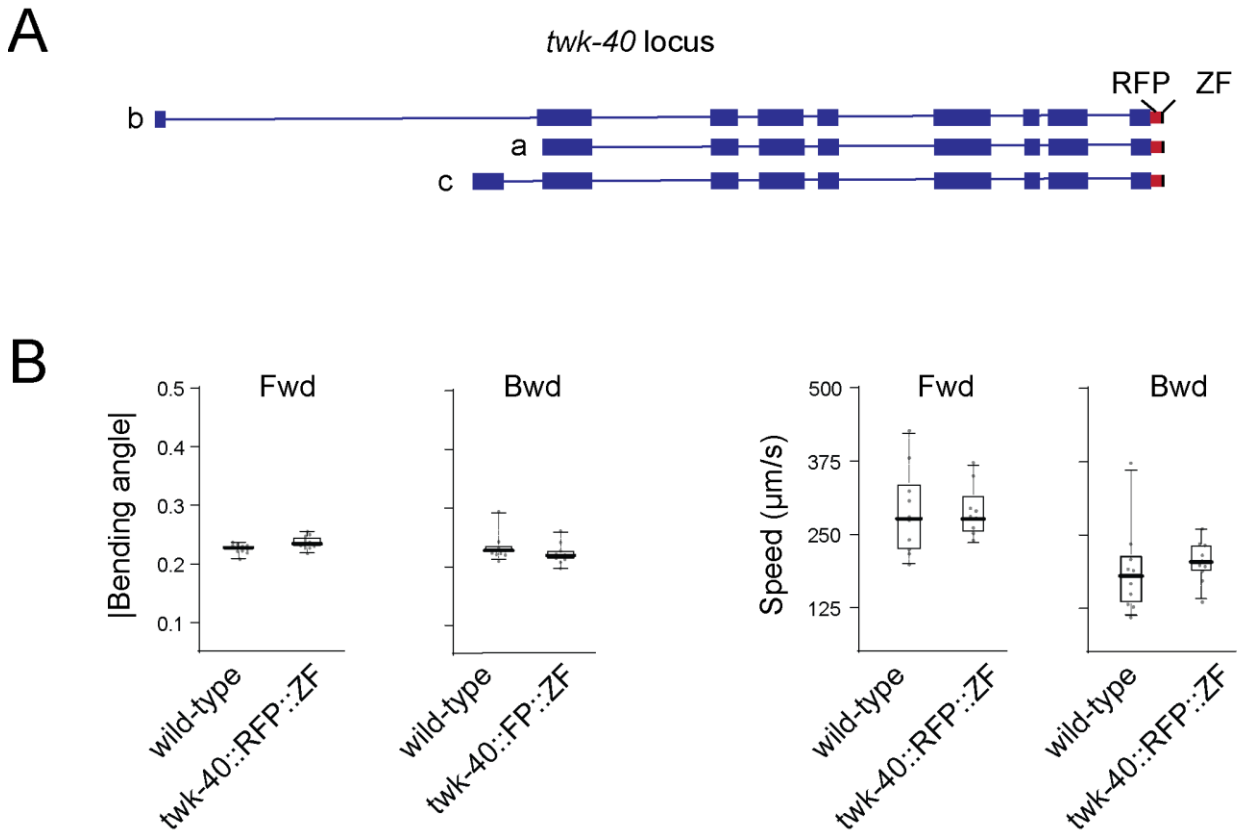

Fig 3S2

Figure 3S2. TWK-40::RFP::ZF knockin animals exhibit wildtype motor behaviors

A. Genomics structures of the *twk-40* gene, with three predicted protein isoforms (a, b, and c). Blue boxes and lines denote exons and introns, respectively. Red and green boxes denote an C-terminal in-frame insertion of the TagRFP and ZF domains in the endogenous *twk-40* genomic locus. **B.** Mean absolute bending angles (left) and centroid speed (right) of wild-type animals (N: 11) and *twk-40::TagRFP::ZF* animals (N: 11). Box-whisker plot displays the 90/10 and 75/25 percentiles, respectively. *: $P < 0.05$, **: $P < 0.01$, ***: $P < 0.001$ by the Mann-Whitney U tests. $P < 0.05$ is considered to be statistically significant.

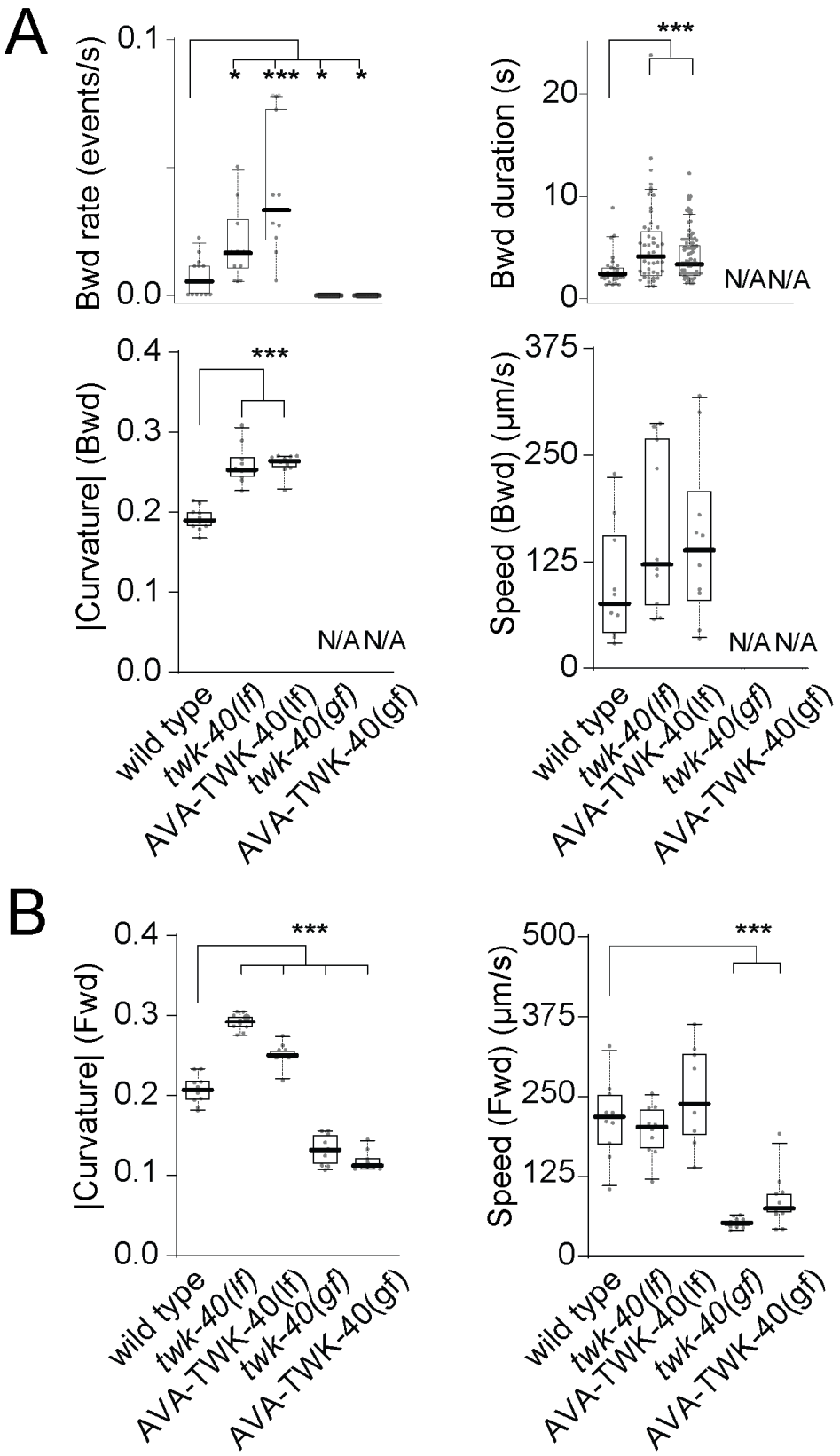
A
Bwd rate (events/s)
0.1
0.0
* *** * *
Bwd duration (s)
20
10
0
***
N/AN/A
|Curvature| (Bwd)
0.4
0.3
0.2
0.1
0.0
***
N/A N/A
Speed (Bwd) (µm/s)
375
250
125
0
N/A N/A
wild type
twk-40(lf)
AVA-TWK-40(lf)
twk-40(gf)
AVA-TWK-40(gf)
B
|Curvature| (Fwd)
0.4
0.3
0.2
0.1
0.0
***
Speed (Fwd) (µm/s)
500
375
250
125
0
***
wild type
twk-40(lf)
AVA-TWK-40(lf)
twk-40(gf)
AVA-TWK-40(gf)

Fig 3S3

Figure 3S3. TWK-40 functions mainly through AVA to regulate locomotion

(A) Deceasing and increasing TWK-40 potassium leak led to increased and decreased backward movement. Quantification of (top left) backward movement rate, (top right) duration during backward movement, exhibited by animals of denoted genotypes. *twk-40(lf)* (N: 46 events from 11 animals) and AVA-specific TWK-40(lf) (N: 80 events from 11 animals) animals exhibit increased Backward movement rates and duration compared to wild-type animals (N: 30 events from 13 animals). (Lower left) Mean absolute bending angles and (lower right) centroid speed during backward movement. N: 11 (wild type), 11 (*twk-40(lf)*), 11 (AVA-specific TWK-40(lf)), 11 (*twk-40(gf)*) and 12 (AVA-specific TWK-40(gf)) animals. **(B)** (Left) mean absolute bending angles and (right) centroid speed during forward movement by animals of denoted genotypes. N: 11 (wild-type), 11 (*twk-40(lf)*), 11 (AVA-specific TWK-40(lf)), 11 (*twk-40(gf)*) and 12 (AVA-specific TWK-40(gf)) animals. N/A: no events. Box-whisker plot displays the 90/10 and the 75/25 percentiles, respectively. *: $P < 0.05$, **: $P < 0.01$, ***: $P < 0.001$ by the Mann-Whitney U tests. $P<0.05$ is considered to be statistically significant.

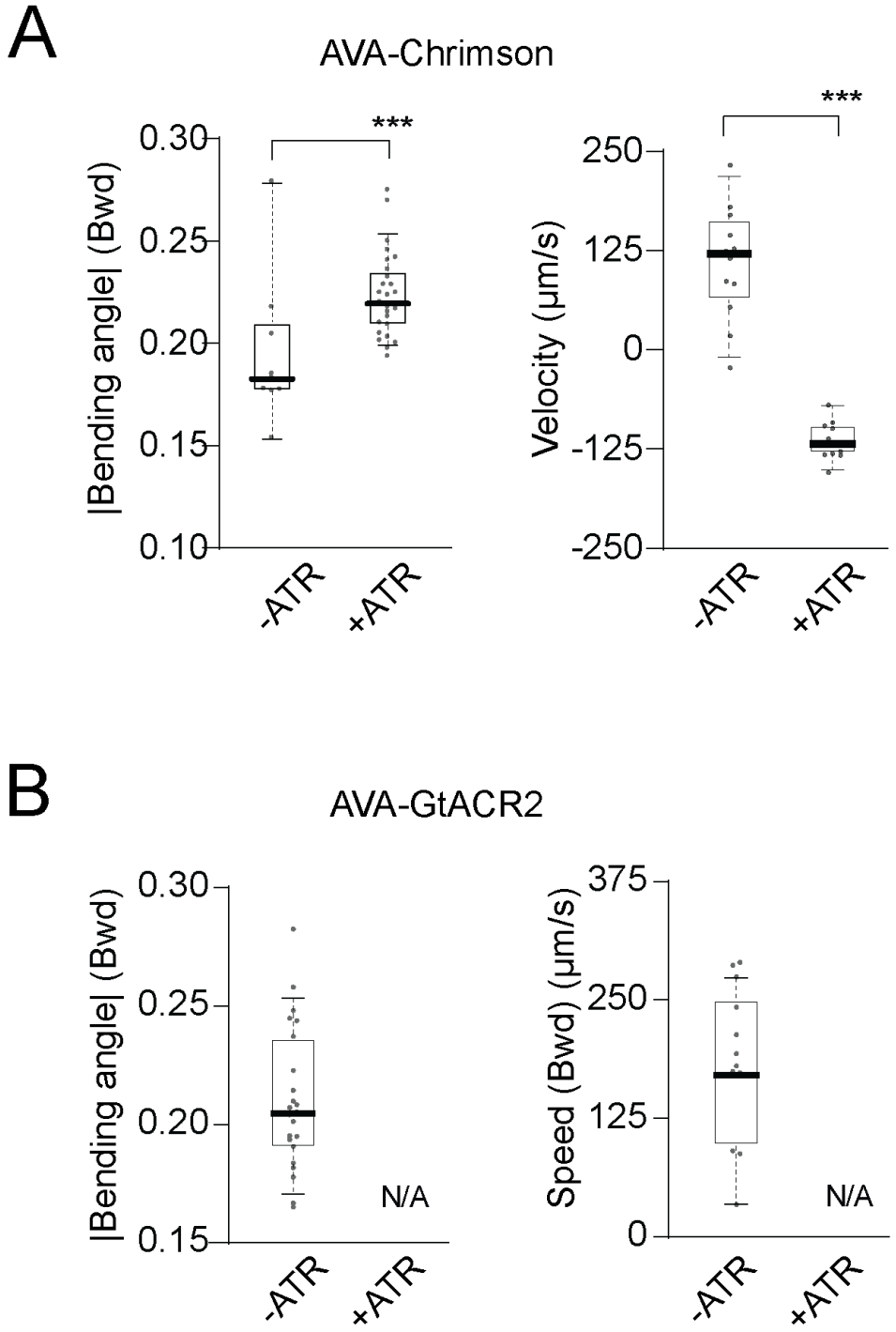
A
AVA-Chrimson
***
***
|Bending angle| (Bwd)
0.30
0.25
0.20
0.15
0.10
Velocity (µm/s)
250
125
0
-125
-250
-ATR
+ATR
-ATR
+ATR
B
AVA-GtACR2
|Bending angle| (Bwd)
0.30
0.25
0.20
0.15
N/A
Speed (Bwd) (µm/s)
375
250
125
0
N/A
-ATR
+ATR
-ATR
+ATR

Fig 3S4

Figure 3S4. Optogenetic manipulation of AVA regulates the backward movement

A. Quantification of the backward movement, by the mean absolute bending angles (left) and centroid velocity (right), in non-stimulated (-ATR) (N: 28) and stimulated (+ATR) (N: 25) animals that express activating opsin Chrimson specifically in AVA. Acute AVA depolarization potentiates instantaneous backward movement. **B.** Quantification of the backward movement, by the mean absolute bending angles (left) and centroid speed (right), in non-stimulated (-ATR) (N: 12) and stimulated (+ATR) (N: 10) animals that express inhibitory opsin GtACR2 specifically in AVA. Backward movement was immediately and acutely blocked during stimulation. N/A: no events. Box-whisker plot displays the 90/10 and the 75/25 percentiles respectively. *: $P < 0.05$, **: $P < 0.01$, ***: $P < 0.001$ by the Mann-Whitney U tests. $P < 0.05$ is considered to be statistically significant.

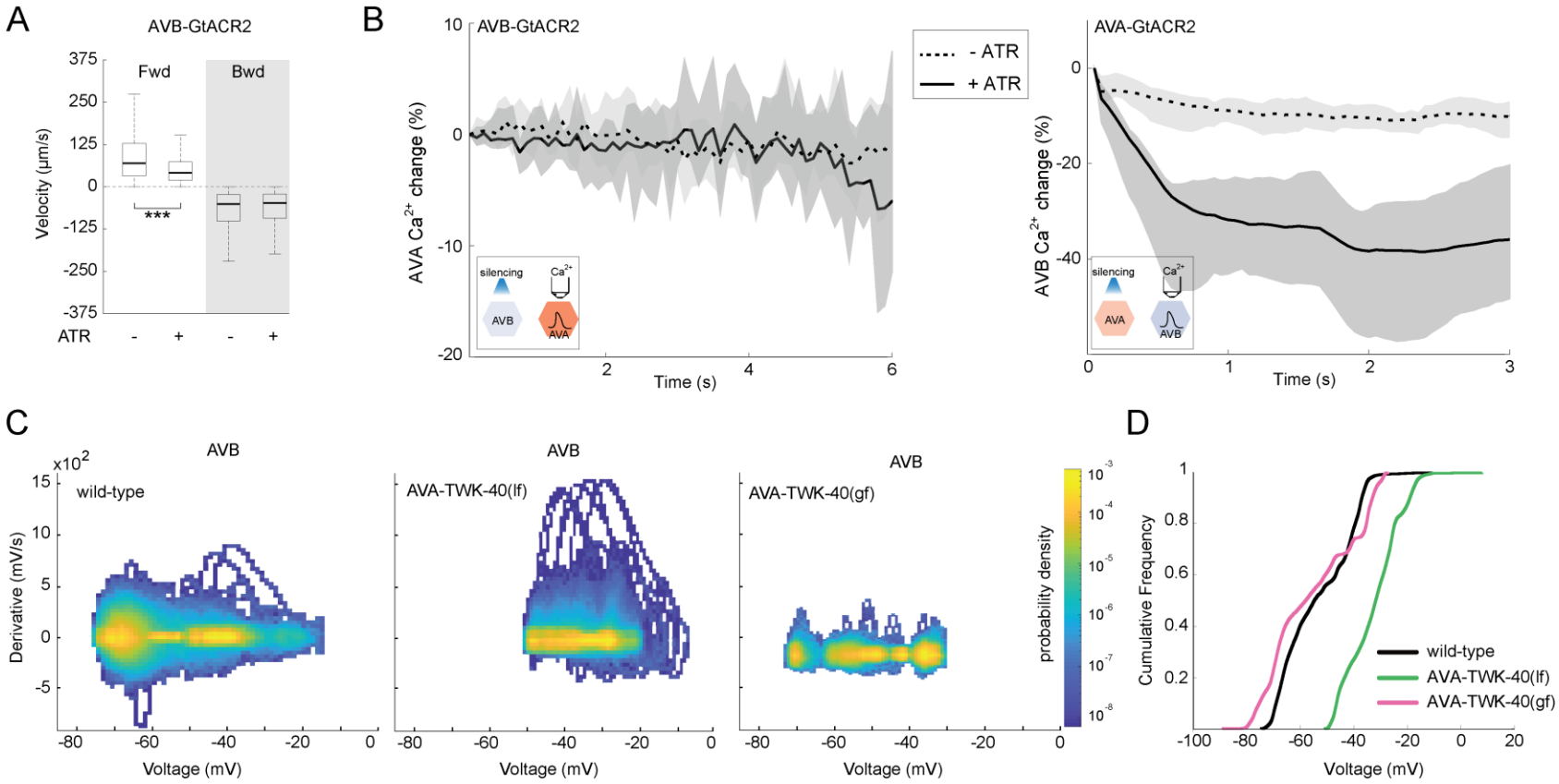
A
AVB-GtACR2
Fwd
Bwd
Velocity (µm/s)
375
250
125
0
-125
-250
-375
***
ATR
-
+
-
+
B
AVB-GtACR2
AVA Ca2+ change (%)
10
0
-10
-20
Time (s)
2
4
6
- ATR
+ ATR
silencing
Ca2+
AVB
AVA
AVA-GtACR2
AVB Ca2+ change (%)
0
-20
-40
Time (s)
0
1
2
3
C
AVB
wild-type
x10^2
Derivative (mV/s)
15
10
5
0
-5
Voltage (mV)
-80
-60
-40
-20
0
AVA-TWK-40(lf)
AVA-TWK-40(gf)
probability density
10^-3
10^-4
10^-5
10^-6
10^-7
10^-8
D
Cumulative Frequency
1
0.8
0.6
0.4
0.2
wild-type
AVA-TWK-40(lf)
AVA-TWK-40(gf)
-100
-80
-60
-40
-20
0
20
Voltage (mV)

Fig 4

Figure 4. AVA potentiation of AVB is largely unidirectional

A. Quantification of mean velocity upon optogenetic inhibition of AVB by GtACR2. Silencing AVB led to decreased forward speed without affecting backward speed (ATR+; N: 11) compared to non-stimulated animals (-ATR; N: 5). **B.** (Left) AVA calcium activity in immobilized animals upon optogenetic inhibition of AVB by GtACR2. Inactivation of AVB (+ATR; N: 28) did not lead to consistent changes in AVA calcium dynamics compared to un-stimulated animals (-ATR; N: 19). (Right) AVB calcium activity in immobilized animals upon optogenetic inhibition of AVA. Inactivation of AVA (+ATR; N: 23) led to reduced AVB calcium dynamics compared to un-stimulated animals (-ATR; N: 23). Lines and shaded bars denote the median and 95% confidence interval, respectively. Insert panels illustrate the experimental setup. **C.** Distribution of the voltage derivative across AVB membrane potential in respective genotypes. In AVA-specific TWK-40(*lf)* (N: 7) and AVA-specific TWK-40(*gf*) (N: 7) mutant animals, AVB exhibited an increased and decreased voltage dynamic range, respectively, compared to wild-type animals (N: 8). **D.** Cumulative curves of AVB membrane potential, where the AVB neuron exhibited a more depolarized and hyperpolarized potential range in AVA-specific *twk-40(lf)* (N: 7) and AVA-specific *twk-40(gf)* (N: 7) mutant animals, respectively, compared to wild-type animals (N: 7).

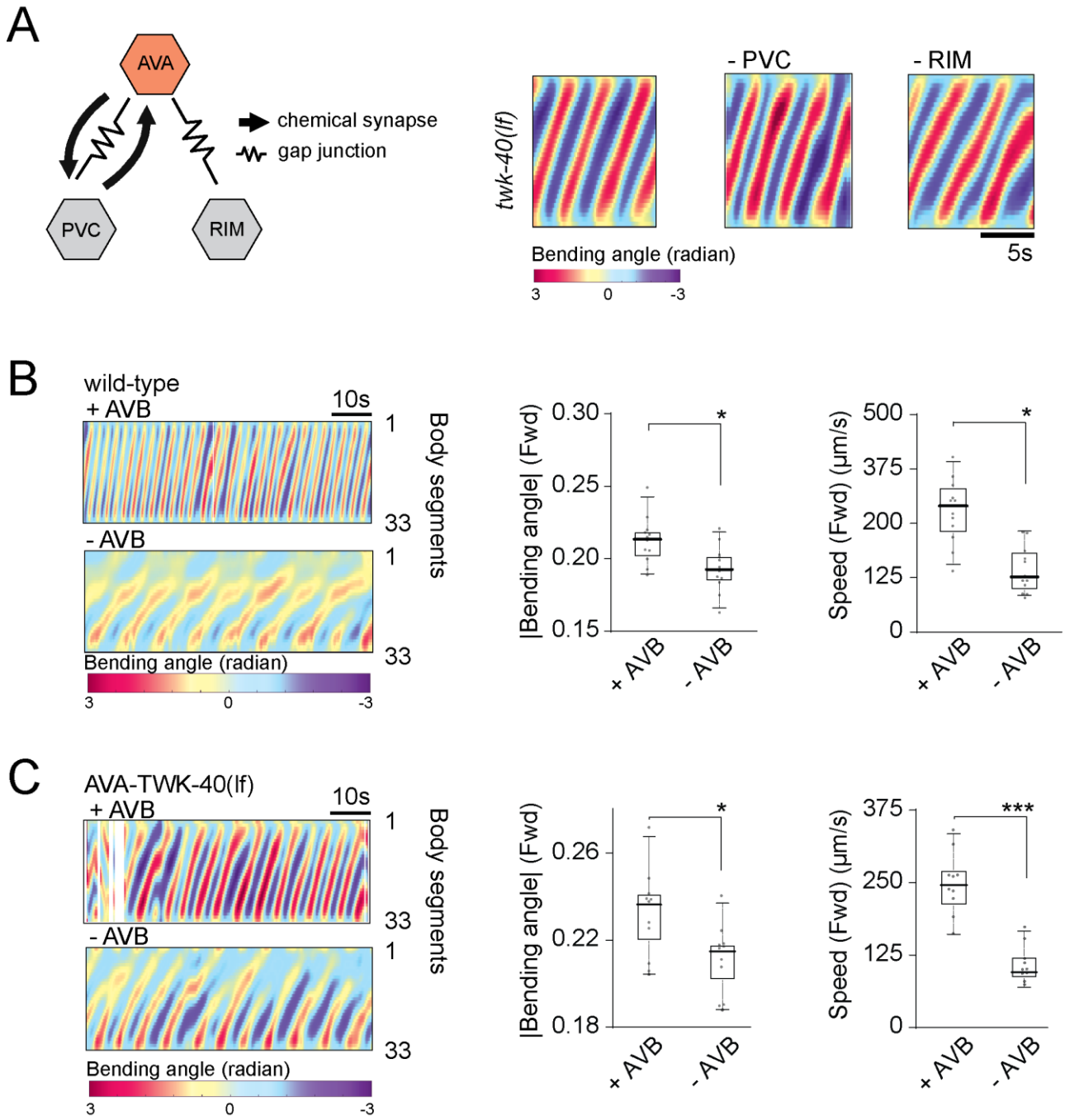
A
AVA
PVC
RIM
chemical synapse
gap junction
twk-40(lf)
- PVC
- RIM
Bending angle (radian)
3
0
-3
5s
B
wild-type
+ AVB
10s
1
33
Body segments
- AVB
1
33
Bending angle (radian)
3
0
-3
|Bending angle| (Fwd)
0.30
0.25
0.20
0.15
*
+ AVB
- AVB
Speed (Fwd) (µm/s)
500
375
200
125
0
*
+ AVB
- AVB
C
AVA-TWK-40(lf)
+ AVB
10s
1
33
Body segments
- AVB
1
33
Bending angle (radian)
3
0
-3
|Bending angle| (Fwd)
0.26
0.22
0.18
*
+ AVB
- AVB
Speed (Fwd) (µm/s)
375
250
125
0
***
+ AVB
- AVB

Fig 4S1

Figure 4S1. AVA-mediated potentiation of the forward movement requires AVB

A. (Left) Anatomic wiring diagram of other neurons that make consistent chemical and gap junctional connections with AVA, adapted from[23,78,79]. (Right) Representative kymograph of *twk-40(lf)* mutant animal's bending angles during forward movement, upon anatomic ablation of neurons of PVC or RIM, There were no significant changes in the bending angle or centroid speed. **B.** Anatomic ablation of AVB in wild-type animals led to significantly reduced forward bending angles and centroid forward speed. (Left) Representative kymographs of the bending angles of wildtype (control, +AVB; N: 13) and AVB ablated (-AVB) animals (N: 13). (Right) Mean absolute bending angles and centroid speed during the forward movement by animals of respective genotypes. **C.** Ablation of AVB led to significantly reduced bending angles and centroid speed during forward movement of AVA-specific TWK-40(lf) animals. (Left) Representative kymographs of bending angles of Control (+AVB, N: 11) and AVB ablated (-AVB) animals (N: 11) in AVA-specific TWK-40(lf) mutant animals. (Right) Mean absolute bending angles and centroid speed during the forward movement by animals of respective genotypes. Box-whisker plot displays the 90/10 and 75/25 percentiles, respectively. *: $P < 0.05$, **: $P < 0.01$, ***: $P < 0.001$ by the Mann-Whitney U tests. $P<0.05$ is considered to be statistically significant.

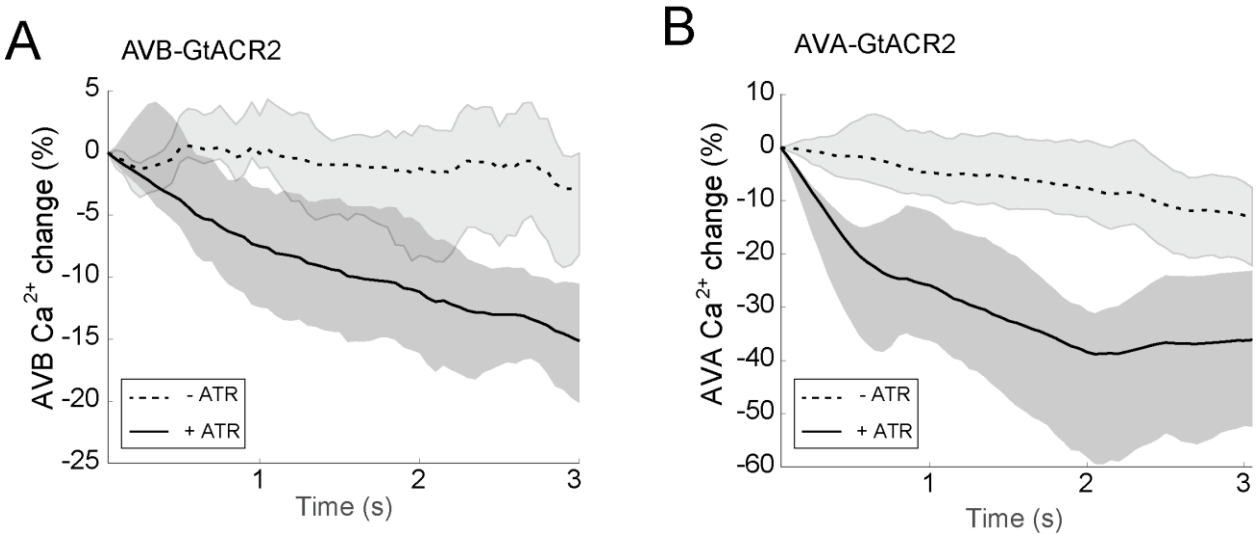

Fig 4S2

Figure 4S2. AVB-specific GtACR2 and AVA-specific GtACR2 are functional

A. Optogenetic inhibition of AVB by AVB-specific GtACR2 in immobilized animals led to reduced AVB calcium activity (+ATR; N: 28) compared to un-stimulated (-ATR; N: 19) animals. Lines and shaded bars denote the median and 95% confidence internal, respectively. **B.** Optogenetic inhibition of AVA by AVA-specific GtACR2 in immobilized animals led to reduced AVA calcium activity (+ATR; N: 23) compared to un-stimulated (-ATR; N: 23) animals. Lines and shaded bars denote the median and 95% confidence interval, respectivel

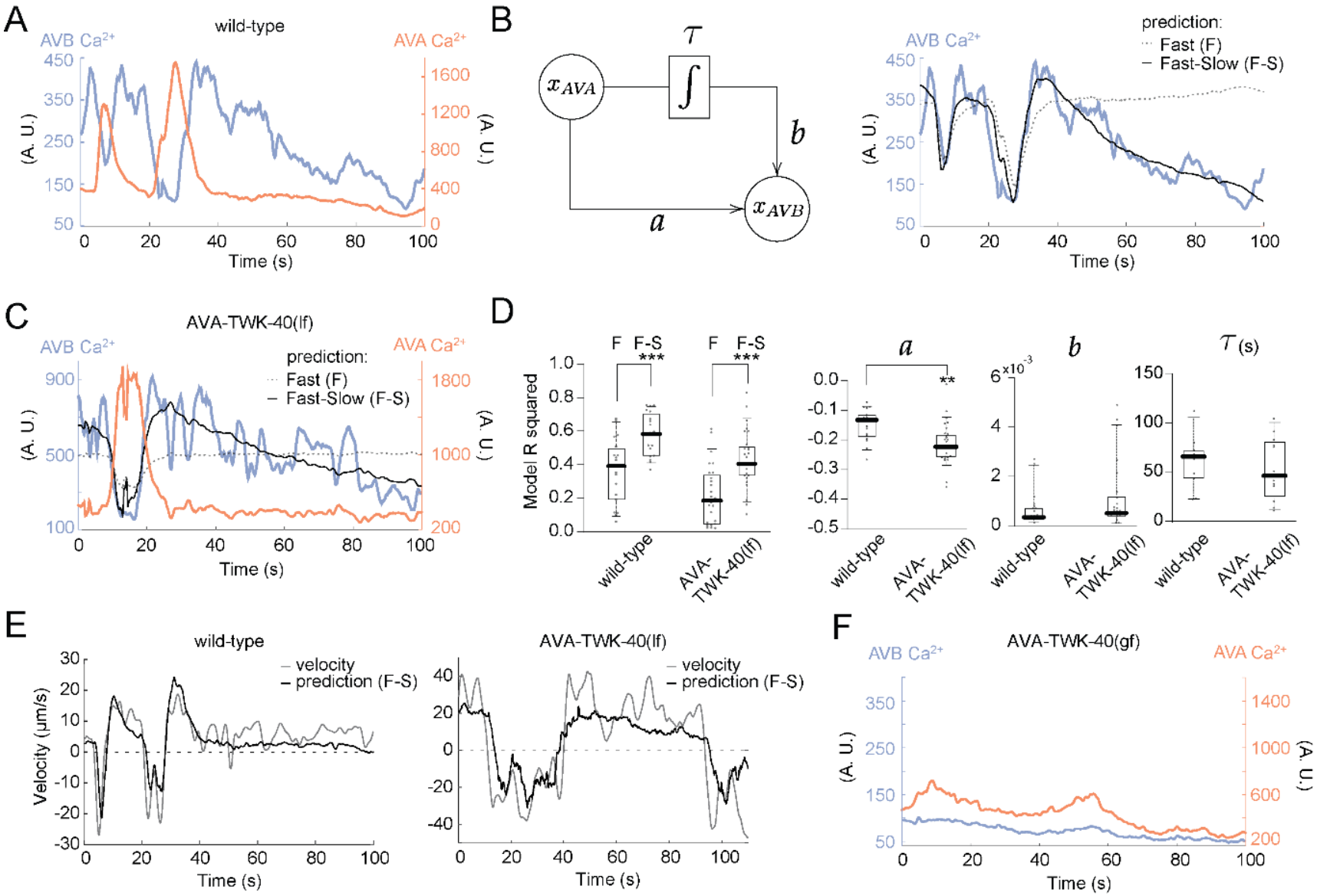
A
wild-type
AVB Ca2+
AVA Ca2+
(A. U.)
Time (s)
B
τ
x_{AVA}
x_{AVB}
a
b
prediction:
Fast (F)
Fast-Slow (F-S)
C
AVA-TWK-40(lf)
D
Model R squared
F
F-S
***
**
a
b
τ (s)
wild-type
AVA-TWK-40(lf)
E
velocity
prediction (F-S)
Velocity (μm/s)
F
AVA-TWK-40(gf)

Fig 5

Figure 5. A two-time scale model predicts AVA and AVB's relationship

A. Representative calcium imaging traces of co-imaged AVA and AVB during spontaneous movements by a wild-type animal. **B.** (Left) AVB activity is modeled as a sum of two terms dependent on AVA's activity. A fast copy with a proportionality constant *a* and a slow copy integrated with a timescale τ and proportionality constant *b*. (Right) The fast-slow model is a better fit for AVB's post-backward movement activity compared to a model without the slow timescale. **C.** Example calcium traces of AVA and AVB from AVA-specific TWK-40(lf) mutant animals show that the fast-slow model also explains AVB's activity when AVA was further depolarized. **D.** (Left panel) Model R-squared values comparing the fast-slow model with the fast only models, for both wild-type and AVA-specific-TWK-40(lf) animals. Removing the slow time scale input decreases model performance in both cases. (Right panels) Comparison of the estimated value for parameters for *a*, *b,* and τ (the integration timescale for the slow copy) between wild-type and AVA-specific TWK-40(lf) traces. Biologically, the two-time scale model suggests a fast inhibition (negative *a*) and a slow excitation (positive *b*) from AVA to AVB. N: wild-type - 11 epochs of backward movement from 11 animals; AVA-specific TWK-40(lf) - 10 epochs of backward movement from 10 animals. Box-whisker plot displayed the 90/10 and 75/25 percentiles, respectively. *: $P < 0.05$, **: $P < 0.01$, ***: $P < 0.001$ by the Mann-Whitney U tests. $P < 0.05$ is considered to be statistically significant. **E.** Sample traces of the F-S model prediction of the velocity of (left) wild-type animals and (right) AVA-specific TWK-40(lf) mutant animals from AVA calcium activity. Parameters: wild-type $a = -0.51$,$b = 0.02$, $\tau = 3.5$s; AVA-specific TWK-40(gf): $a = -0.38$, $b = 0.004$, $\tau = 16.6$s. **F.** Representative calcium activity traces of co-imaged AVA and AVB by a freely moving AVA-Specific-TWK-40(gf) mutant animal. Both neurons showed strong reduction in activity.

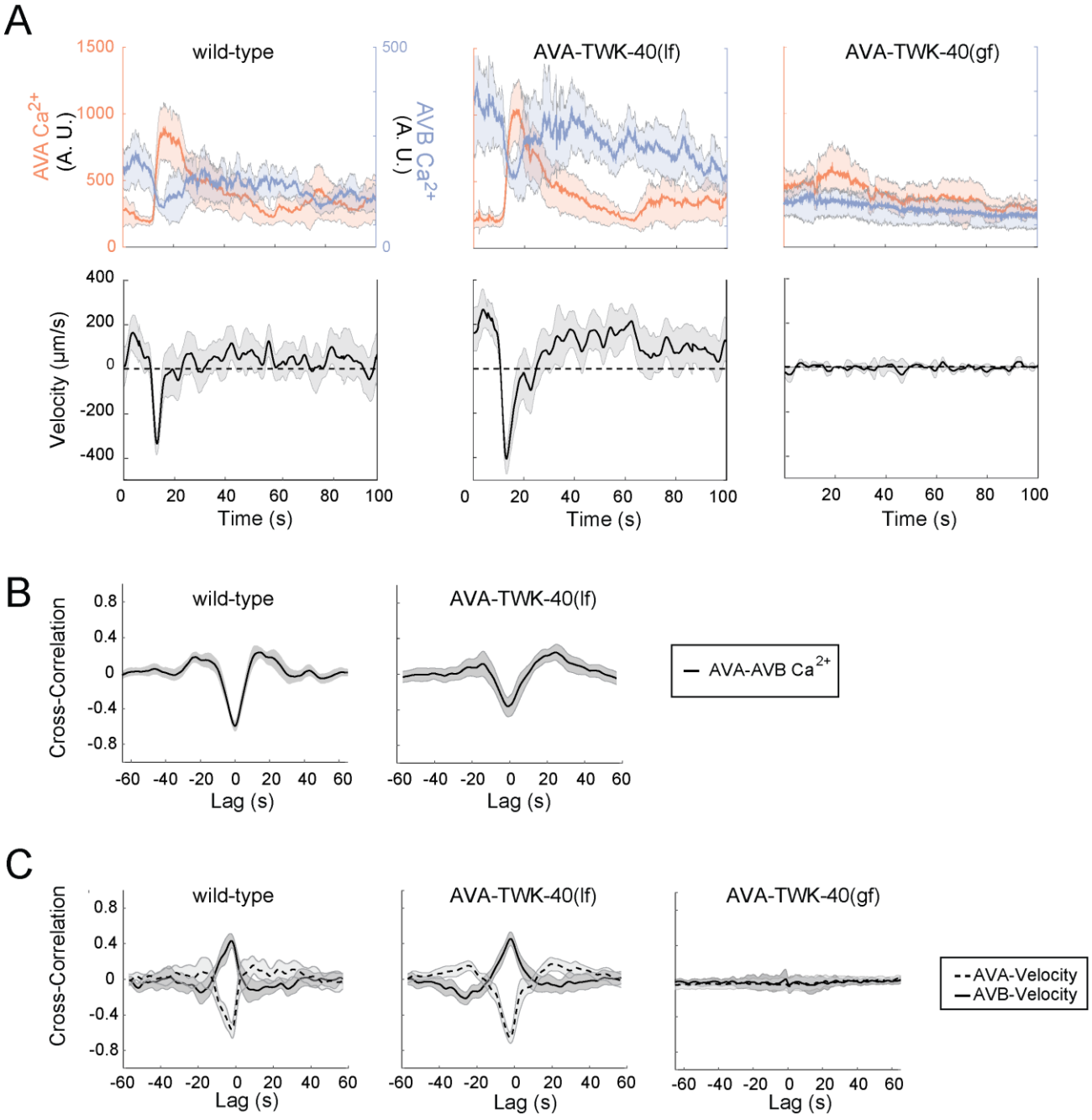
A
wild-type
AVA-TWK-40(lf)
AVA-TWK-40(gf)
AVA Ca2+ (A. U.)
AVB Ca2+ (A. U.)
Velocity (µm/s)
Time (s)
B
Cross-Correlation
Lag (s)
AVA-AVB Ca2+
C
AVA-Velocity
AVB-Velocity

Fig 5S

Figure 5S. AVA's activity is required to main the forward movement

A. (Upper panels) Mean calcium activity of AVA and AVB, aligned to the start of an AVA transient for wild-type, AVA-specific TWK-40(lf), and AVA-specific TWK-40(gf) animals, respectively. (Lower panels) Centroid velocities corresponding to the upper traces. + and – denote forward and backward movements, respectively. N: wild-type (19 epochs, from 11 animals); AVA-specific TWK-40 (27 epochs from 10 animals); AVA-specific TWK-40(gf) (4 epochs from 4 animals). Lines and shaded bars indicate the mean and 95% confidence interval. **B.** Mean cross-correlations between AVA and AVB's calcium activity for wild-type (left panel) and AVA-specific TWK-40(lf) mutant (right panel) animals. **C.** Mean cross-correlations between AVA calcium activity and centroid velocity, and AVB calcium activity and centroid velocity for wild-type animals (Left panel), AVA-specific TWK-40(lf) mutants (Middle panel), and AVA-specific TWK-40(gf) mutants (Right panel). In both wild-type and AVA-specific TWK-40(lf) mutants, AVA calcium activity exhibited a negative correlation with backward speed during backward movement, and a weaker positive correlation with forward speed post-backward movement.

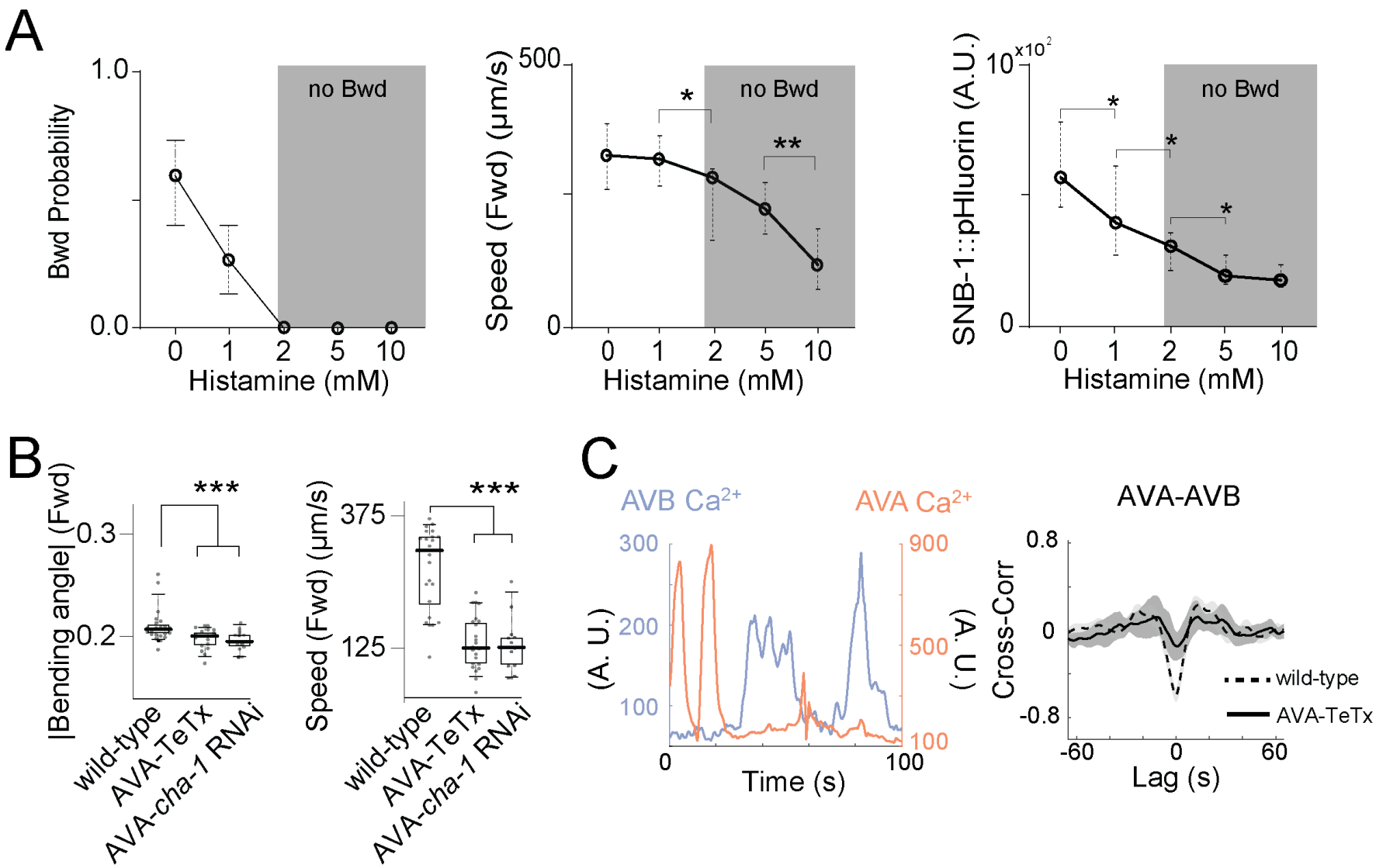
A
Bwd Probability
1.0
0.0
no Bwd
0 1 2 5 10
Histamine (mM)
Speed (Fwd) (µm/s)
500
0
*
**
no Bwd
0 1 2 5 10
Histamine (mM)
SNB-1::pHluorin (A.U.)
10x10²
0
*
*
*
no Bwd
0 1 2 5 10
Histamine (mM)
B
|Bending angle| (Fwd)
0.3
0.2
***
wild-type
AVA-TeTx
AVA-cha-1 RNAi
Speed (Fwd) (µm/s)
375
125
***
wild-type
AVA-TeTx
AVA-cha-1 RNAi
C
AVB Ca2+
AVA Ca2+
300
200
100
(A. U.)
900
500
100
(A. U.)
0
100
Time (s)
AVA-AVB
Cross-Corr
0.8
0
-0.8
wild-type
AVA-TeTx
-60
0
60
Lag (s)

Fig 6

Figure 6. Tonic acetylcholine release from AVA potentiates forward movement

A. (Left) Backward movement probability upon inhibition of AVA by HisCl at different histamine concentrations. Histamine impaired spontaneous backward movement in a dosage-dependent manner. N: 15 animals at each concentration. (Middle) Centroid forward speed upon inhibition of AVA by HisCl at different histamine concentrations. The forward speed exhibited a gradual reduction upon increased histamine. N: 15 animals per concentration. (Right) Mean AVA-specific SNB-1::pHluorin signals upon inhibition of AVA by HisCl at different histamine concentrations. While showed a continuous decrease with increased histamine concentration. While the spontaneous backward movement was already fully blocked at 2mM histamine, fluorescent signals persisted, and continuously decrease with increased histamine. N: 30 (0mM), 29 (1mM), 30 (2mM), 31 (5mM), 28 (10 mM) animals. Shaded areas denote Histamine's concentration range where we observed complete abolishment of spontaneous backward movement. Quantification showed median and 95% confidence interval. **B.** Mean absolute bending angles (Left panel) and mean centroid speed (Right panel) during forward movement by animals with AVA's synaptic vesicle fusion blocked (AVA-TeTx), or vesicular acetylcholine loading blocked (AVA-*cha-1* RNAi). Forward movements were reduced by AVA-specific TeTx and AVA-*cha-1* RNAi. N: 23 animals (Control), 18 animals (AVA-specific TeTx), 14 animals (AVA-*cha-1* RNAi). Box-whisker plot displays the 90/10 and 75/25 percentiles, respectively. **C.** (Left panel) Representative traces of co-imaged AVA and AVB calcium activity in a freely moving AVA-specific TeTx animal. (Right panel) Mean cross-correlations of co-imaged AVA and AVB activity in wild-type and AVA-specific TeTx animals. Positive and negative correlation with the backward speed and post-backward forward speed, respectively, exhibited by wild-type animals, were both reduced in AVA-specific TeTx animals. N: 32 epochs from 10 AVA-specific TeTx animals; 21 epochs from 11 wild-type animals. *: $P < 0.05$, **: $P < 0.01$, ***: $P < 0.001$ by the Mann-Whitney U tests. $P < 0.05$ is considered to be statistically significant.

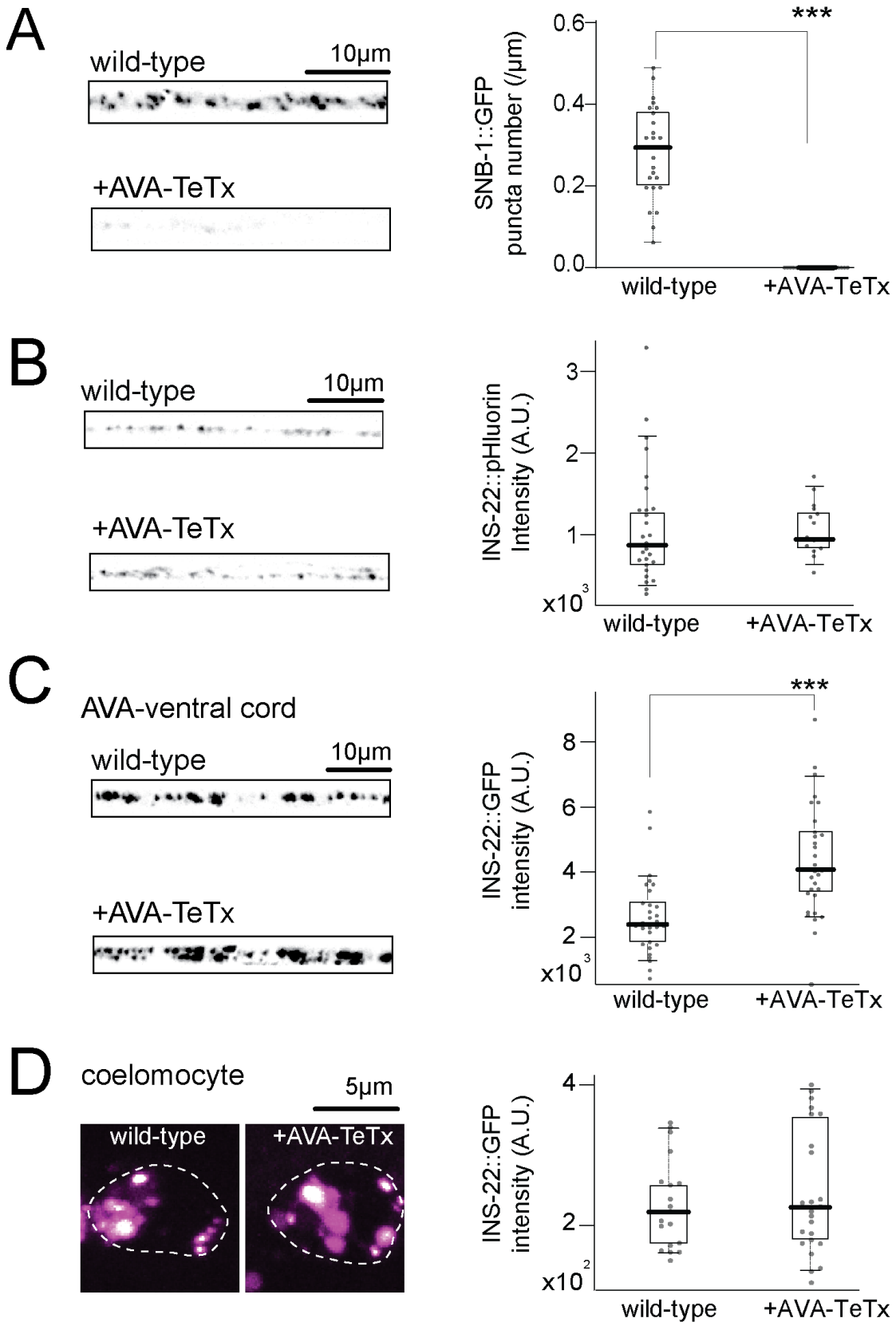
A
wild-type
10µm
+AVA-TeTx
SNB-1::GFP puncta number (/µm)
0.6
0.4
0.2
0.0
***
wild-type
+AVA-TeTx
B
wild-type
10µm
+AVA-TeTx
INS-22::pHluorin Intensity (A.U.)
3
2
1
x10^3
wild-type
+AVA-TeTx
C
AVA-ventral cord
wild-type
10µm
+AVA-TeTx
INS-22::GFP intensity (A.U.)
8
6
4
2
x10^3
***
wild-type
+AVA-TeTx
D
coelomocyte
5µm
wild-type
+AVA-TeTx
INS-22::GFP intensity (A.U.)
4
2
x10^2
wild-type
+AVA-TeTx

Fig 6S1

Figure 6S1. Tetanus toxin (TeTx), commonly used to block chemical synaptic transmission[103,104], cleaves synaptobrevin and preferentially blocks AVA's chemical synaptic transmission.

A. In AVA, TeTx potently cleaves SNB-1. Representative confocal images (Left panels) and quantifications of AVA-specific SNB-1::GFP signals (Right panel) in animals that express AVA-specific TeTx. SNB-1::GFP signals were diminished by the presence of TeTx. N: 22 AVA-TeTx animals and 25 wild-type animals. **B.** TeTx has a minor effect on neuropeptide secretion from AVA. Representative confocal images (Left panels) and quantification of fluorescent signals (Right panel) from an ectopically expressed INS-22::pHluorin from AVA showed no significant change in the presence of TeTx. N: 15 AVA-TeTx animals and 27 wild-type animals. **C.** Representative confocal images (Left panels) and quantification of fluorescent signals of AVA-specific neuropeptide INS-22::GFP marker (Right) showed increased intensity in the presence of AVA-specific TeTx. N: 30 AVA-TeTx animals and 30 wild-type animals. **D.** Representative images (Left panels) and quantification of secreted INS-22::GFP signals (Right), which accumulated in the coelomocytes. Mean INS-22::GFP intensity exhibited a wider range in AVA-TeTx animals (N: 26) but did not lead to a statistically significant difference with that of the wild-type animals (N: 20). Box-whisker plot displays the 90/10 and 75/25 percentiles, respectively. *: $P < 0.05$, **: $P < 0.01$, ***: $P < 0.001$ by the Mann-Whitney U tests. $P<0.05$ is considered to be statistically significant.

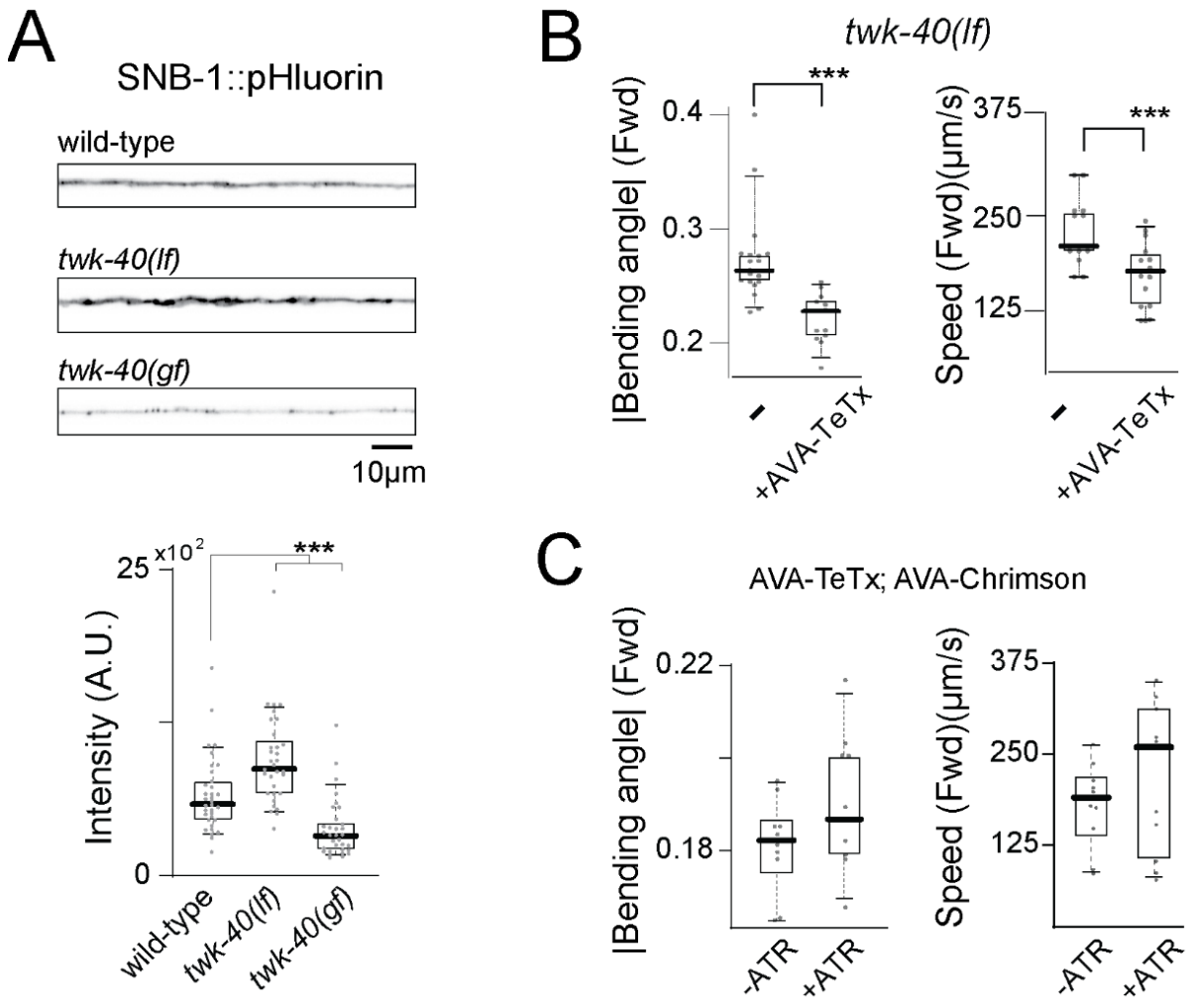
A
SNB-1::pHluorin
wild-type
twk-40(lf)
twk-40(gf)
10µm
25
x10^2
***
Intensity (A.U.)
0
wild-type
twk-40(lf)
twk-40(gf)
B
twk-40(lf)
***
|Bending angle| (Fwd)
0.4
0.3
0.2
-
+AVA-TeTx
***
Speed (Fwd)(µm/s)
375
250
125
-
+AVA-TeTx
C
AVA-TeTx; AVA-Chrimson
|Bending angle| (Fwd)
0.22
0.18
-ATR
+ATR
Speed (Fwd)(µm/s)
375
250
125
-ATR
+ATR

Fig 6S2

Figure 6S2. Acetylcholine release from AVA maintains the forward movement

A. Representative confocal images (Upper panels) and quantification (lower panel) of AVA-specific SNB-1::pHluorin signals in wild-type animals (N: 34), *twk-40(lf)* mutants (N: 32), and *twk-40(gf)* mutants (N: 32). pHluorin signals were significantly increased and decreased in *twk-40(lf)* and *twk-40(gf)*, respectively, compared to wild-type animals. **B.** Mean absolute bending angles (left panel) and centroid speed (right panel) during the forward movement by animals with synaptic vesicle fusion blocked (AVA-TeTx) in *twk-40(lf)* animals. The forward movement was reduced by AVA-specific TeTx. N: 20 *twk-40(lf)* and 14 AVA-TeTx; *twk-40(lf)* animals. **C.** Mean absolute bending angles (left panel) and centroid speed (right panel) of the forward movement upon AVA's constitutive optogenetic activation (+ATR), in the presence of TeTx. Stimulation. They were compared with animals of the same genotype, treated with the same treatment but without opsin-activation (-ATR). When synaptic vesicle fusion was blocked, constitutive stimulation of AVA did not potentiate forward movement. N: 10 (-ATR) and 11 (+ATR) animals. Box-whisker plot displays the 90/10 and the 75/25 percentiles, respectively. *: $P < 0.05$, **: $P < 0.01$, ***: $P < 0.001$ by the Mann-Whitney U tests. $P<0.05$ is considered to be statistically significant.

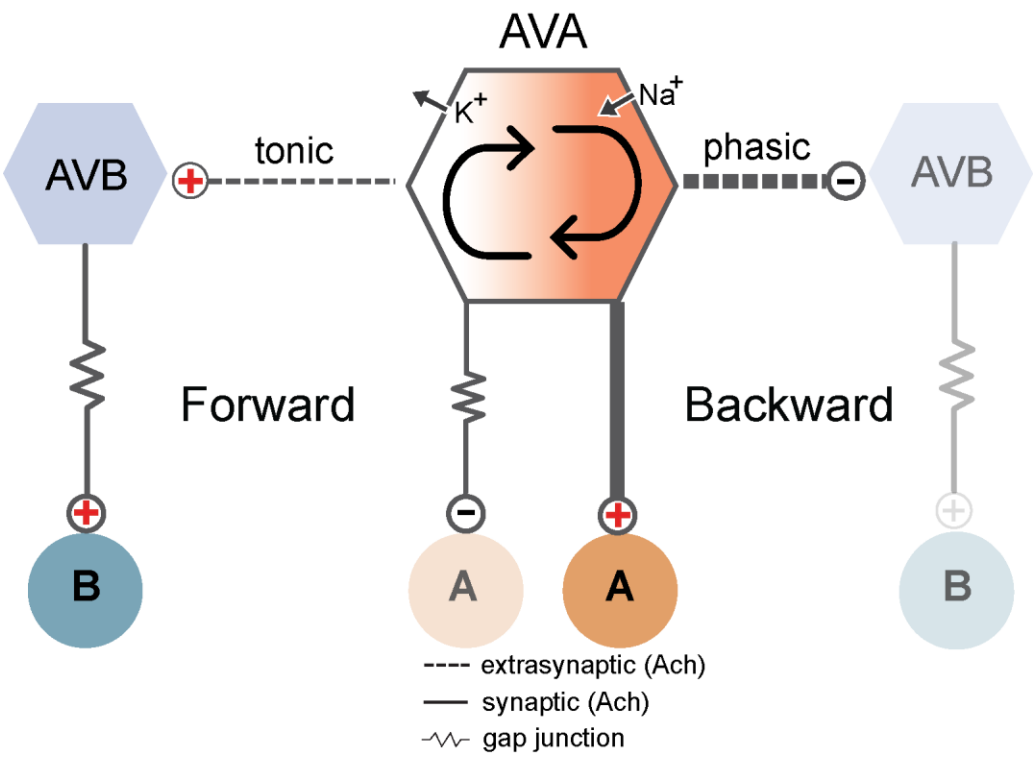

Figure 7. A master neuron configuration for continuous modulation and transitions between directional movements

AVA functions as a master regulator to coordinate the forward and backward movement and their smooth transitions. This modulatory neuron depends on cyclic changes of AVA activity. **(Left)** At its lower activity state, AVA actively shunts the backward motor neurons A by gap junction-coupling[28]. At this state, AVA's tonic potentiation of AVB, which activates the forward motor neurons B[29,62], dominates. This ensures sustained forward movement. **(Right)** At its high activity state, AVA phasically activates the backward motor neurons A by chemical synaptic transmission[28]. At this state, AVA exerts phasic inhibition of AVB, which initiates and sustains the backward movement. Arrows between the low and high AVA states denote continuous modulations of AVA activity during transitions between the mutually exclusive forward and backward motor states. Dashed and solid lines denote extrasynaptic(indirect) and synaptic connectivity, respectively; thickness denotes communication strength.

Movie S1. In wildtype animals, ablation of PVC or RIM did not change the bending curvature or velocity during spontaneous movement.

Representative movies of freely moving animals with or without ablation of either PVC or RIM neurons. Non ablated refers to wild-type background animals carrying the respective miniSOG transgene for PVC or RIM ablation, but without the light exposure that activates ablation. Ablation of PVC or RIM led to increased backward frequency, but did not disrupt the smooth transitions between the forward and backward motor states.

Movie S2. In *twk-40(lf)* mutant animals, ablation of PVC or RIM did not reduce the increased bending curvature, speed, or transitions between the forward and backward motor states.

Representative movies of freely moving animals with or without ablation of either PVC or RIM neurons in *twk-40(lf)* mutant animals. *twk-40(lf)*; non ablated refers to *twk-40(lf)* mutant animals carrying the respective miniSOG transgene for PVC or RIM ablation, but without the light exposure that activates ablation.

Table 1: Membrane potentials (MP) of *C. elegans* neurons

Neuron class	Neuron	Approximate 'Rest' MP
Sensory neuron	AFD	-40 mV[98,105], -80 mV[92]
Sensory neuron	AWA	-75 mV[92,106]
Sensory neuron	PLM	-60 mV[97]
Sensory neuron	ASE	-55 mV[37] -60mV[107]
Sensory neuron	ASH	-60 mV[95]
Interneuron	AIY	-55 mV[92]
Interneuron	AIA	-80 mV[108]
Premotor interneuron	AVA	-20 to -30 mV[40–42]
Premotor interneuron	AVB	-75 to -55 mV (this study)
Premotor interneuron	AVE	-35 mV (S. Gao, unpublished)
A *sra-11* expressed neuron	unsure	-20 mV[109]
Motor neuron	RMD	-70 mV and -35 mV[42]
Motor neuron	RIM	-40 mV[92]
Enteric motor neuron	DVB	-60 mV[93]
Enteric motor neuron	AVL	-40 mV[93]
Motor neuron	VA5	-70 mV[43]
Motor neuron	VB6	-50 mV[43]
Motor neuron	VD5	-45 mV[43]

Table 2. Strains and constructs generated and/or used in this study

Strain	Genotype	Plasmid	Description (see Notes)	Figures
Electrophysiology recording (visualization of AVA and AVB)				
ZM11177	*hpIs860*	pJH4693	*[Ptwk-40s-eGFP; *Pmyo-2-wCherry]*	1B-D; 3A; 3S1
ZM11207	*twk-40(bln336); hpIs860*	pJH4693	*twk-40(gf); [Ptwk-40s-eGFP; *Pmyo-2-wCherry]*	3A; 3S1
ZM11208	*twk-40(hp834); hpIs860*	pJH4693	*twk-40(lf); [Ptwk-40s-eGFP; *Pmyo-2-wCherry]*	3A; 3S1
ZM11145	*hpIs768/+; hpEx4405*	pJH4316 pJH4237 pJH4693	AVA- specific TWK-40(gf) *[Pflp-18LoxPstopLoxPtwk-40(L202N)::GFP Pnmr-1-FLP]; [Ptwk-40s-eGFP; *Pmyo-2-wCherry]*	4C, D
ZM11139	*twk-40(bln282) hpEx3904; hpEx4401*	pJH4018 pJH2673 pJH4693	AVA-specific TWK-40(lf) *twk-40::TagRFP::ZF [Prig-3-FRT-stop FRT twk-40(gf); Ptwk-40s-FLP, *HygR] [Ptwk-40s-eGFP; *Pmyo-2-wCherry]*	4C, D
***twk-40* mutants and locomotion characterization**				
ZM8302	*twk-40(hp834)*	CRISPR/ Cas9	*twk-40(lf)*	2B; 3S3
JIP1514	*twk-40(bln336)*	CRISPR/ Cas9	*twk-40(gf)*	2B; 3S3
JIP1368	*twk-40(bln282)*	CRISPR/ Cas9	*twk-40::TagRFP::ZF*	3S2
ZM10113	*twk-40(bln282); hpIs727*	pJH3830	AVA-specific TWK-40(lf) *twk-40::TagRFP::ZF; [Prig-3-zif-1 sl2 RFP; *Pttx-3-GFP]*	3B; 3S3
ZM10066	*hpEx4053*	pJH4203 pJH2673	AVA- specific TWK-40(gf) *[Prig-3-FRTstopFRT twk-40(L202N)::GFP Pnmr-1-FLP; *Pmyo-2-wCherry]*	3B; 3S3
Immunostaining				
ZM10355	*twk-40(bln282); hpEx4120*	pJH1371	*twk-40::TagRFP::ZF; [Prgef-1-GPI::YFP]*	2C
PVC ablation				
ZM7054	*hpIs321*	pJH2827	AVA, AVE, AVD, RIM, PVC mini SOG *[Pnmr-1-tomm-20::miniSOG sl2 wCherry; *Lin-15(+)]*	4S1A
RIM ablation (RIM miniSOG)				

ZM7978	*hpIs327*	pJH2829	*[Pcex-1-tomm-20::miniSOG sl2 wCherry; *Lin-15(+)]*	4S1A
AVA-specific TeTx and *cha-1* RNAi				
ZM10755	*hpIs814*	pJH4508 pJH4237	AVA-specific TeTx *[Pflp-18-LoxP EBFP stop LoxP TeTx::RFP ; Ptwk-40s-Cre]*	6B
ZM11082	*twk-40 (hp834) ; hpIs814*	pJH4508 pJH4237	*twk-40(lf);* *[Pflp-18-LoxP EBFP stop LoxP TeTx:RFP; Ptwk-40s-Cre]*	6S2B
ZM11086	*hpEx4362*	PCR product	AVA-specific *cha-1* RNAi *[Pflp-18-cha-1(sense); Ptwk-40-cha-1 (antisense); *Pttx-3-GFP]*	6B
AVA peptide secretion and synaptic vesicle analyses				
ZM11039	*hpEx4351*	pJH4677	*[Pnpr-4-ins-22::GFP]*	6S1C, D
ZM11078	*hpEx4351;* *hpEx4364*	pJH4677 pJH4506	with AVA-TeTx *[Pnpr-4-ins-22::GFP];* *[Pnpr-4-TeTx-wCherry]*	6S1C, D
ZM11084	*hpEx4363*	pJH4687	*[Pnpr-4-ins-22::pHluorin; *Pmyo-2-wCherry]*	6S1B
ZM11085	*hpEx4363;* *hpIs814*	pJH4687 pJH4508 pJH4237	with AVA-TeTx *[Pnpr-4-ins-22::pHluorin; *Pmyo-2-wcherry];* *[Pflp-18-LoxP EBFP Stop LoxP TeTx::RFP; Ptwk-40s-Cre]*	6S1B
ZM10040	*hpIs721*	pJH4169 pJH2673	AVA-specific vesicle marker *[Prig-3 FRT stop FRT SNB-1::GFP; Pnmr-1-FLP; *Pmyo-2-wcherry]*	6S1A
ZM10786	*hpIs721;* *hpIs811*	pJH4169 pJH2673 pJH4508 pJH4237	with AVA-TeTx *[Prig-3 FRT stop FRT SNB-1::GFP; Pnmr-1-FLP; *Pmyo-2-wCherry];* *[Pflp-18-LoxP EBFP Stop LoxP TeTx::RFP; Ptwk-40s-Cre]*	6S1A
ZM11287	*hpEx4479*	pJH4783	*[Pnpr-4-SNB-1::pHluorin; *Lin-15]*	6S2A
ZM11284	*twk-40(bln336); hpEx4479*	pJH4783	*twk-40(gf);* *[Pnpr-4-SNB-1::pHluorin; *Lin-15]*	6S2A
ZM11285	*twk-40 (hp834); hpEx4479*	pJH4783	*twk-40(lf);* *[Pnpr-4-SNB-1::pHluorin; *Lin-15]*	6S2A
AVA optogenetic (Chrimson) activation				
ZM10206	*hpIs758*	pJH4253 pJH4237	*[Prig-3 LoxP EBFP stop LoxP Chrimson::RFP; Ptwk-40s-Cre]*	3B; 3S4A
ZM11151	*hpIs758;* *hpIs814*	pJH4253 pJH4237 pJH4508 pJH4237	with AVA-TeTx *[Prig-3-LoxP EBFP stop LoxP Chrimson::RFP; Ptwk-40s-Cre];* *[Pflp-18-LoxP EBFP stop LoxP TeTx::RFP; Ptwk-40s-Cre]*	6S2C

AVA HisCl chemogenetic inactivation				
ZM9354	*hpIs636*	Ref.[36]	*[Prig-3::HisCl1::SL2::mCherry]*	6A, left/mid
ZM11286	*hpIs636;* *hpEx4479*	Ref.[36] pJH4783	*[Prig-3::HisCl1::SL2::mCherry];* *[Pnpr-4-SNB-1::pHluorin; *Lin-15]*	6A, right panel
AVA optogenetic (GtACR2) inactivation				
ZM10806	*hpIs824*	pJH4562 pJH4237	*[Pflp-18-LoxP EBFP stop LoxP gtACR2::RFP;* *Ptwk-40s-Cre]*	3D; 3S4B
ZM10538	*hpIs774;* *hpEx4081*	pJH4293 pJH4217 pJH4237	<u>with AVA/AVB co-calcium imaging</u> *[Ptwk-40s-GCaMP6s::mNeptune]* *[Prig-3 LoxP EBFP Stop LoxP gtACR2::RFP;* *Ptwk-40s-Cre]*	4B, 4S2B
AVB optogenetic (GtACR2) inactivation				
ZM10942	*lin-15(n765);* *hpIs774;* *hpEx4292*	pJH4293 pJH4609 pJH4237	<u>with AVA/AVB co-calcium imaging</u> *[Ptwk-40s-GCaMP6s::mNeptune];* *[Ppdf-1 LoxP eBFP LoxP gtACR2::wCherry;* *Ptwk-40s-Cre; *Lin-15(+)]*	4A, B 4S2A
AVB ablation (AVB miniSOG)				
ZM7297	*hpIs331*	pJH2890	*[Plgc-55-mito::miniSOG UrSL wCherry;* **Lin-15(+)]*	4S1B
ZM10327	*twk-40(bln282);* *hpIs331;* *hpIs727*	pJH2890 pJH3830	<u>with AVA-specific TWK-40(lf)</u> *twk-40::TagRFP::ZF;* *[Plgc-55-mito::miniSOG sl2 RFP; *Lin-15];* *[Prig-3-zif-1 sl2 RFP]*	4S1C
AVA-AVB co-calcium imaging				
ZM10767	*hpIs819*	pJH4542	*[Ptwk-40s-GCaMP T2A nls::mNeptune;* **LIN-15(+)]*	5A, B, D, E; 5S
ZM11014	*twk-40(bln282);* *hpIs819;* *hpEx3904*	pJH4542 pJH4018 pJH2673	<u>with AVA-specific TWK-40(lf)</u> *twk-40::TagRFP::ZF;* *[Ptwk-40s-GCaMP:T2A:nls:RFP; *Lin-15];* *[Prig-3 sl2 FRT EBFP FRT zif-1;* *Pnmr-1-FLP; *HygR]*	5C-E; 5S
ZM11015	*hpIs819;* *hpIs768*	pJH4542 pJH4316 pJH4237	<u>with AVA-specific TWK-40(gf)</u> *[Ptwk-40s-GCaMP:T2A:nls:RFP; *Lin-15];* *[Pflp-18LoxPEBFPstopLoxP twk-40(L159N)::GFP* *Ptwk-40s-Cre]*	5F; 5SA, C
ZM11034	*hpIs819;* *hpIs810*	pJH4542 pJH4508 pJH4237	<u>AVA-specific TeTx</u> *[Ptwk-40s-GCaMP:T2A:nls:RFP; *Lin-15];* *[Pflp-18-LoxP EBFP Stop LoxP TeTx::RFP;* *Ptwk-40s-Cre]*	6C
*Notes: [ ] integrated (Is) or extra-transgenic (Ex) arrays; * Co-injection markers; Stop: stop codon or termination sequence in the let-858 3' UTR.*				

Methods

Constructs and strains

A full list of constructs and stains used in this study is shown in Table 2. Constructs and strains are available at the Addagene, the *CGC* center, or upon request. All *C. elegans* strains were cultured on the standard Nematode Growth Medium (NGM) plates seeded with OP50 and maintained at 22.5 °C unless specified. The wild-type animal refers to the Bristol N2 strain or control animals as specified in figure legends. L4 stage hermaphrodites were used for all experiments unless specified otherwise.

Isolation, cloning, and generation of *twk-40* mutants and AVA-specific TWK-40 alleles

The first *twk-40* loss-of-function(lf) allele, *hp733*, was isolated in a genetic screen based on altered motor behavior. *hp733* was isolated with exaggerated amplitude in both forward and reverse movement as well as a tendency to form a backward coil. *hp733* was mapped to the left arm of chromosome III past the SNP marker W06F12 at ~-21. Whole genome sequencing revealed a single missense mutation TWK-40(E36K) in *hp733* animals. Fosmids and plasmids containing the wild-type *twk-40* coding sequence fully rescued the motor phenotypes of *hp733*. We subsequently generated another *twk-40* lf allele, *hp834,* using CRISPR gene editing. *hp834* has a 7bp deletion in between exon 1 and the following intron (base 3378-3384 (GTTCGAG) of T28A8.1b), resulting in a frame-shift mutation of *twk-40* coding sequence that is predicted to translate only the first twelve amino acids of the channel. *twk-40(hp834)* mutant animals displayed motor behaviors of similar characteristics but more severe than that of *twk-40(hp733)* mutants. *hp834* was the canonical *lf* allele used for all experiments shown in this study.
Gain-of-function(gf) allele, *bln336(L181N)* was engineered by CRISPR/Cas9 editing by mutating the 4298-4299 base of T28A8.1b from CT to AA[51]. Cell-specific TWK-40 degradation was generated by a repurposed ZIF E3 ligase degradation system[110]. *bln282 (twk-40::TagRFP::ZF)* was generated by CRISPR/Cas9 genome editing to insert an C-terminal TWK-40 in frame TagRFP::ZF fusion at base pair 5785 at T28A8.1b[100].
AVA-specific TWK-40(lf) animals were generated by expressing the ZIF E3 ligase specifically in AVA using the *Prig-3* or *Pnmr-1*/*Prig-3* combination (*Prig-3 FRT zif-1 sl2 eBFP FRT; Pnmr-1-FLP*) via the FRT-FLP recombination system in *bln282 (twk-40::Tag RFP::ZF)*.
AVA-specific TWK-40(gf) animals were generated by expressing TWK-40(L181N)::GFP specifically in AVA by P*flp-18*/P*twk-40* combination (*Pflp-18-LoxP stop LoxP twk-40(gf)::GFP; Ptwk-40-cre*) via the Cre-LoxP recombination system in the N2 background,

or P*rig-3*/P*nmr-1* combination (*Prig-3-FRT stop FRT twk-40(gf)::GFP; Pnmr-1-FLP*) via the FRT-FLP recombination system or (*Pflp-18-LoxP stop Loxp twk-40(gf)::GFP; Ptwk-40-cre*) via the cre-Lox recombination system in N2 background. AVA-specific TWK-40 rescue was generated by expressing wildtype TWK-40(WT)::GFP specific in AVA by *Prig-3*/P*nmr-1* combination (*Prig-3 FRT Stop FRT twk-40::GFP; Pnmr-1-FLP*) via the FRT-FLP recombination system in *twk-40(lf)* background.

Spontaneous locomotion analyses

A single L4 animal was collected and transferred to an NGM plate with a thin layer of evenly spread OP50. After 30 seconds, it was recorded on a tracking microscope using an in-house developed ImageJ plugin[26]. A 3-minute movie for each animal was recorded at 10 fps. At least 10 animals for each genotype were recorded on the same day using the same condition. Movies were analyzed as previously described[28,61]. Briefly, the animal contour was divided into 33 segments by its centerline along the longitudinal axis. Body curvature in radian was calculated between adjacent segments for segments 5-32. Velocity was calculated by the displacement of the centroid.

Electrophysiology

Exogenous TWK-40 channel whole-cell patch recording in HEK293 cells: HEK293 cells were cultured in the DMEM medium with 10% fetal bovine serum, 1% double antibody at 5% CO_2, and 37°C. TWK-40 expression construct was generated by RT-PCR amplification of cDNA b isoform and inserting into the BstXI and NheI sites of the pCDNA3.1 vector. After 24 hours of transfection of the plasmid with the liposome ExFect2000 (Vazyme, China), cells were patched using 4-6 MΩ-resistant borosilicate pipettes (1B100F-4, World Precision Instruments, USA). Pipettes were pulled by micropipette puller P-1000 (Sutter, USA), and fire-polished by microforge MF-830 (Narishige, Japan). Membrane currents and I-V curve were recorded and plotted in the whole-cell configuration by pulse software with the EPC-9 amplifier (HEKA, Germany) and processed with the Igor Pro (WaveMetrics, USA) and Clampfit 10 software (Axon Instruments, Molecular Devices, USA). I-V curve was recorded at a holding potential from –80 mV to 80 mV with 20 mV step voltages. Data were digitized at 10-20 kHz and filtered at 2.6 kHz. The pipette solution contained (in mM): KCl 140; $MgCl_2$ 1; EGTA 10; HEPES 10; Na_2ATP 4; pH 7.3 with KOH, ~300 mOsm. The bath solution consisted of (in mM): NaCl 140; KCl 3.6; $CaCl_2$ 2.5; $MgCl_2$ 1; pH 7.3 with NaOH, ~310 mOsm. For low intracellular K^+ recording, the pipette solution contained (in mM): KCl 14; CsCl 126; $MgCl_2$ 1; EGTA 10; HEPES 10; Na_2ATP 4; pH 7.3 with CsOH, ~300 mOsm. Chemicals were

obtained from Sigma unless stated otherwise. Experiments were performed at room temperatures (20-22°C).

in situ whole-cell patch clamp of C. elegans neurons AVA and AVB: Premotor interneuron whole-cell patch clamp recording was performed using a strain with fluorescent labeling of AVA and AVB neurons, a configuration as previously described[28,41], which was modified from previous reports[42,46,111]. Briefly, 1- or 2-day-old hermaphrodite adults were glued (Histoacryl Blue, Braun) to a sylgard-coated cover glass covered with bath solution (Sylgard 184, Dowcorning) under a stereoscopic microscope (M50, Leica). After clearing the viscera by suction through a glass pipette, the cuticle flap was turned and gently glued down using WORMGLU (GluStitch Inc.) to expose the soma of AVA and AVB neurons. Neurons were patched using ~20 MΩ-resistant borosilicate pipettes (1B100F-4; World Precision Instruments). Pipettes were pulled by micropipette puller P-1000 (Sutter) and fire-polished by microforge MF-830 (Narishige). Membrane currents and potentials were collected in the whole-cell configuration by pulse software with an EPC9 amplifier (HEKA, Germany). Data were digitized at 10 kHz and filtered at 2.6 kHz. The recording pipette solution consisted of: KCl 25 mM; K-Gluconate 115 mM; $CaCl_2$ 0.1 mM; $MgCl_2$ 5 mM; BAPTA 1 mM; HEPES 10 mM; Na_2ATP 5 mM; Na_2GTP 0.5 mM; cAMP 0.5 mM; cGMP 0.5 mM, pH 7.2 with KOH, ~320 mOsm. cGMP and cAMP were included to increase the longevity of the preparation[41,112]. The bath solution consisted of KCl 5 mM; NaCl 150 mM; $CaCl_2$ 5 mM; $MgCl_2$ 1 mM; glucose 10 mM; sucrose 5 mM; HEPES 15 mM, pH 7.3 with NaOH, ~330 mOsm. The K^+ current was recorded at a holding potential from –60 mV and followed a ramp voltage stimulation from –90 mV to 90 mV. The membrane voltage recording was performed at 0 pA for at least 30 seconds. The background leak currents were recorded at –60 mV. Healthy preparations were selected based on the following criteria: whole-cell capacitance (1-1.5 pF), and steady-state leak current (–20-0 pA at –60mV). Experiments were performed at room temperatures (20-22°C).

Cell ablation by miniSOG

Strains expressing miniSOG[113] in AVB (and other neurons) or RIM (specifically) were used for ablation by exposing the respective L2 larvae to blue LED light as described in previous studies[27,61,114]. Briefly, cells expressing miniSOG were co-labeled with RFP. animals were treated with 30-40 min blue light using a homemade LED device and allowed to recover for 1 day. L4 animals were recorded for behavioral analyses. For PVC ablation, L2 transgenic animals that express miniSOG in multiple premotor interneurons, including but not exclusive to PVC, were anesthetized by sodium azide and mounted onto a 2 percent agarose pad with a coverslip. The tail region, where PVC resides, was

exposed to a blue laser for 30 min and animals were allowed to recover for 2 days before recording at the L4 stage. Only healthy animals were recorded and analyzed. The ablation efficiency and specificity (for PVC) for all experiments was confirmed by the disappearance or distortion of the soma fluorescence and fragmentation of neurites.

Optogenetic stimulation for behavioral and calcium imaging

Strains: Strains that express AVA-specific Chrimson or GtACR2 strains were used for AVA-specific stimulation and inhibition, respectively. The specificity of AVA-specific GtACR2 was verified by AVA ablation using *Pnmr-1*-miniSOG. The AVA-ablated animal no longer exhibited light-induced inhibition during forward and backward movement. Transgenic animals were cultured on ATR plates in darkness for two generations. The second-generation L4-stage animals were analyzed for behavior and calcium activities. Controls were animals of the same genotypes, cultured and treated similarly, except with no ATR included on culture plates.
Behaviors upon stimulation: an individual L4-stage animal was transferred to an imaging plate with a thin layer of evenly spread OP50. LED light stimulation were applied to inhibit or activate AVA, by activating GtACR2 or Chrimson, respectively as below.
GtACR2-mediated AVA inactivation: Animals were cultured on with or without ATR-supplemented NGM plates for 2 hours. During stimulation, L4 stage animals were exposed to 470nm LED light (Thorlabs) at low intensity (4 out of 63 A.U.) with a 10 second pre-stimulation, 10 seconds stimulation and 10 second post stimulation cycle.
GtACR2-mediated AVB inactivation: L4 stage AVB-specific GtACR2 animals were incubated on plates with or without -ATR or +ATR (1ml OP50 /5µl 50µM ATR) plates for 2 hours and then subjected to behavior recording with a constant 470nm LED light (Thorlabs) exposure at low intensity (4 out of 63 A.U.) for 800 seconds.
Chrimson-mediated AVA activation: Animals were cultured on with or without ATR-supplemented NGM plates for at least 1 day for behavior recording. During stimulation, L4 stage animals were exposed to 574nm LED light (Thorlabs) at low intensity (63 out of 63 A.U.) with a 10 second pre-stimulation, 10 seconds stimulation and 10 second post stimulation cycle..
Constitutive, moderate Chrimson-mediated AVA activation: with or without ATR-supplemented NGM plates were seeded with regular OP50 supplemented with ATR (1ml OP50/0.5µl 50µm ATR). Animals were cultured on plates for at least 1 day for behavior recording. Before recording, (L4 stage) AVA were constitutively activated by 544nm green LED light for up to 5min (Zeiss V16), followed by recording at 595nm LED (Thorlabs) at low intensity (4 out of 63 A.U.).

Simultaneous calcium recording and optogenetic stimulation: The experiment process was previously described[114]. Briefly, L4 stage animals carrying AVA and AVB calcium reporters and either AVA-specific GtACR2 or AVB-specific GtACR2 were incubated on -ATR or +ATR plates for 2 hours. They were immobilized on dry agarose pads in M9 buffer and subjected to full spectrum light illumination for simultaneous calcium imaging and GtACR2-mediated inhibition at 10 fps or 20 fps for 6-20 seconds.

Behavioral analyses upon chemogenetic manipulation

Animals of the L4 stage carrying an integrated chromosomal array for *Prig-3* HisCl::mCherry[36] were incubated on 0mM, 2mM, 5mM, or 10mM histamine plates with OP50 for 1 hour before being individually placed on the behavioral imaging plates for spontaneous behavior recording and quantification.

Immunofluorescent staining and imaging

Mixed stages of animals with endogenously tagged *twk-40* (*twk-40*::TagRFP::ZF), with or without the plasma marker (*Prgef*-1-GPI::YFP), and animals with an integrated *twk-40::GFP* fosmid were fixed in 2% paraformaldehyde at 4°C for 1 hour and processed as previously described[115]. Primary antibodies against TagRFP (Thermo Fisher Scientific, R10367, rabbit) and/or GFP (Roche, mouse) were used at 1:500 and 1:200 dilution, respectively. Secondary antibodies of goat-anti-rabbit (Alexa Fluor 488) and/or goat anti-mouse (Alexa Fluor 594) were used at 1:5000 dilution. L4 larvae and adults were imaged with a Nikon spinning disk confocal microscope with a 63x objective and reconstructed by maximum intensity projection. Single layers of acquired images from animals co-expressing TWK-40::TagRFP::ZF and GPI::YFP were examined for subcellular colocalization using an ImageJ plugin (JACoP).

Live fluorescence microscopy of GFP and pHluorin

Live L4 larvae were immobilized on dry agarose pads in a small drop of M9 buffer. Fluorescence signals were captured using Nikon Eclipse 90i confocal microscope and Nikon Eclipse T12 with Yokogawa CSU-X1 spinning disk field scanning confocal system. For pHluorin imaging, all images were acquired within 10min after dry pad preparation. All fluorescent images were analyzed by the in-house developed puncta analyzer[116] or ImageJ intensity analyzer.

Calcium imaging of premotor interneurons in moving animals

For AVA (L or R) and AVB (L or R) co-imaging, an individual transgenic L3 stage animal expressing the GCaMP6s calcium sensor in AVA and AVB (*hpIs819*) was mounted on a 2

percent NGM gel pad with ~1µl M9 buffer so that it could move under a coverslip. Mounted animals were allowed to recover for 3min on the pad before recording. The recording was performed using a 20x objective on Nikon spinning disk confocal microscope. Animals were centered in the field of view by manual tracking. AVB soma was manually kept in focus at the RFP channel during recording. The initiation of each epoch of backward to forward locomotion transition was defined by the alignment between velocity and AVA-AVB calcium activity (GCaMP intensity) using in-house-developed MATLAB scripts[114].

Cell-specific perturbation of neurotransmission

AVA-specific TeTx was achieved by the Cre-LoxP recombination system. AVA-specific *cha-1* RNAi was generated using the combination of P*flp-18* and *Ptwk-40* promoter combination to drive the sense and anti-sense strands of *cha-1* genomic DNA, respectively. The following primers and templates were used:
(A) *Pflp-18*: OZM6199 (GATGGATACGCTAACAACTTGG) and OZM6200 (CTACAACGGCAGCGTATTCGATCCCGTCTAACCCTGAAA) amplified from pJH4631.
(B) *cha-1* exon: OZM6201 (GAATACGCTGCCGTTGTAG) and OZM6240 (GTCGAGTGCTCTATGCACAACC), amplified from N2 genomic DNA.
(C) *Ptwk-40s*: OZM6199 (GATGGATACGCTAACAACTTGG) and OZM6253 (GTATGATGCGACTATTCAGCTGT-GAATATTCATCACTCGATATTCCA) amplified from pJH4608.
(D) *cha-1* exon: OZM6201 (GAATACGCTGCCGTTGTAG) and OZM6202 (CAGCTGAATAGTCGCATCATAC), amplified from N2 genomic DNA.
PCR fusion was performed to obtain sense and anti-sense *cha-1* by following primers*:*
Pflp-18-cha-1(sense): OZM6203 (AGCTTAGCCGGAATAGGGTCA) and OZM6202 (CAGCTGAATAGTCGCATCATAC), amplified from mixed PCR product (A+B).
Ptwk-40-cha-1(antisense): OZM3543 (AATGCGGCCGCTCTAATCACTATCACGT GGGATCTGGATAA); OZM6254 (CGTAG-GCCAGAAAGCCTCAC) from mixed PCR product (C+D). Mixed PCR products were injected into N2 animals.

Modeling

Our approach is to find the simplest phenomenological model (i.e. a non-mechanistic model with as few free parameters as possible) that explains the observed calcium activity patterns of AVA and AVB, as opposed to a detailed, more biologically realistic model. A more realistic model will have several parameters, the estimation of which will require assumptions or experiments to fix.

We first note that our experiments suggest that the communication between AVB and AVA is largely unidirectional, with AVA affecting AVB's activity and very little effect in the opposite direction. Consequently, we start with the following equation for the calcium activity of AVB, x_{AVB}

$$\frac{dx_{AVB}}{dt} = -\frac{1}{\tau_{AVB}} \cdot x_{AVB} + w_{AVA} \cdot \sigma(x_{AVA}) + \Sigma_i w_i \sigma(z_i) + c$$

Where x_{AVA} is the calcium activity of AVA, z_i is the activity of all other input neurons of AVB, w_i is the synaptic weight of each input, c is the bias input, and σ denotes the activation function for the synapse. Typically, the activation function is a sigmoidal function. However, to simplify the model, we restrict our attention to the linear case, where σ is simply the identity function, $\sigma(x) = x$.

Next, we make a key simplification to the model above based on our experiments. Our results show that AVA forms the dominant input on to AVB. Specifically, AVA-twk-40(gf) animals cannot sustain their forward motion (Fig. 2B) and AVB's calcium is significantly reduced in this background (Fig. 3D). This suggests that we can ignore the input from other neurons in the model. Thus, we set $w_i = 0$ for all neurons other than AVA. Giving us the following leaky-integrator differential equation.

$$\frac{1}{w_{AVA}} \frac{dx_{AVB}}{dt} = -\frac{1}{\tau_{AVB} . w_{AVA}} \cdot x_{AVB} + x_{AVA} + c$$

As a final simplification, we assume that the direct input from AVA is faster than the kinetics of the calcium sensor, such that any activity in AVA is immediately reflected in AVB. Thus, we consider the limit $\frac{1}{w_{AVA}} \to 0$. Giving us the final simplified model as

$$x_{AVB} = a \cdot x_{AVA} + c$$

Where $a = \frac{1}{\tau_{AVB} . w_{AVA}}$ is a dimensionless multiplier. As seen in Fig. 5B, this model with $a < 0$ (black dotted line) can predict the anticorrelated activity pattern between AVA and AVB during a backward movement, but is unable to explain AVB's activity after the backward movement.

To capture the slow decay of AVB, we add an additional slower input from AVA to AVB (as shown in the schematic in Fig. 5A). Giving us the following system of equations with just three free parameters.

$$x_{AVB} = a \cdot x_{AVA} + b \cdot y$$

$$\frac{dy}{dt} = -\frac{1}{\tau} \cdot y + x_{AVA}$$

Where, a and b are the coefficients for the fast and slow inputs respectively, and τ is the integration time-constant for the slow component of AVA. To fit the parameters from calcium imaging data, we used *procest* function from MATLAB's system identification toolbox, which estimates the transfer function for the equation above. Laplace transforming the system of equations above results in the following transfer function,

$$\frac{X_{AVB}(s)}{X_{AVA}(s)} = \left[\frac{(a + b \cdot \tau) + (a \cdot \tau) \cdot s}{1 + \tau \cdot s}\right]$$

which has one zero and one pole. The number of zeros and poles form the input to *procest*, along with the calcium traces of AVB calcium (set as output signal) and AVA calcium (set as the input signal). To get a distribution over model parameters and performances, we do a cross-validation procedure where the parameters are estimated from a single recording and then tested on the remaining recordings. The model R-squared showed in Fig 5C shows the distribution from the models thus estimated.
The same setup was used to model the velocity from AVA's calcium activity (Fig 5E) using *procest* (i.e. a single pole, single zero transfer function), with AVA's activity being set as the input signal and velocity forming the output signal.

Statistical analyses

Electrophysiological analyses: The cumulative distributions for the membrane voltage of AVA and AVB were calculated using MATLAB's *ecdf* function. To compute the joint histogram (Fig. 1S1, Fig. 3S2), we first computed the derivative of membrane potential with a finite difference (preceded by smoothing with a Gaussian kernel) and then used MATLAB's bivariate histogram *histogram2* to perform the histogram estimation. For HEK293 cell recording, the Mann-Whitney U tests were used.
Behavior and fluorescent analysis: Mann-Whitney U tests were used to quantify data of box and whisker plots.
Calcium imaging: Error bars in Fig. 4 and Fig. 4S were computed as a 95% confidence interval of the mean bootstrapped over 1000 resamples.
P value less than 0.05 is considered to be statistically significant. *: $P < 0.05$, **: $P < 0.01$, ***: $P < 0.001$.

Conflict of interests

The authors declare no conflict of interest.

Author contributions

Conception and supervision: MZ; Design of experiments, modeling, and analyses: JM, TA, WH, SG, TB, MZ; Data collection: JM, BY, WH, YZ, SG; Reagents and scripts: JM, WH, SM, ZW, YZ, TA, QW; JM, TA and MZ wrote the manuscript; all authors edited or approved the manuscript.

Acknowledgments

We thank Ying Wang and Yan Li for technical support; comments from and discussions with Aravi Samuel, Ben Mulcahy, Miriam Goodman, and Cori Bargmann. This work was supported by the Canadian Institute of Health Research FDN154274 and the Natural Sciences and Engineering Research Council of Canada RGPIN2017-06738 (MZ), the key International (Regional) Joint Research Project (32020103007) (SG and QW), the National Natural Science Foundation of China (31871069) (SG) and the European Research Council (337702-Kelegans) (TB).

References

1. Carreira-Rosario, A. *et al.* MDN brain descending neurons coordinately activate backward and inhibit forward locomotion. *Elife* **7**, (2018).

2. Briggman, K. L. & Kristan, W. B. Imaging dedicated and multifunctional neural circuits generating distinct behaviors. *J. Neurosci.* **26**, 10925–10933 (2006).

3. Mazzucato, L. Neural mechanisms underlying the temporal organization of naturalistic animal behavior. *Elife* **11**, (2022).

4. Briggman, K. L. & Kristan, W. B. Multifunctional pattern-generating circuits. *Annual Review of Neuroscience* **31**, 271–294 (2008).

5. Ramirez, J. M. & Pearson, K. G. Generation of motor patterns for walking and flight in motoneurons supplying bifunctional muscles in the locust. *J. Neurobiol.* **19**, 257–282 (1988).

6. Roberts, W. M. *et al.* A stochastic neuronal model predicts random search behaviors at multiple spatial scales in C. elegans. *Elife* **5**, (2016).

7. Berkowitz, A. Both shared and specialized spinal circuitry for scratching and swimming in turtles. *J. Comp. Physiol. A. Neuroethol. Sens. Neural. Behav. Physiol.* **188**, 225–234 (2002).

8. Gaudry, Q., Ruiz, N., Huang, T., Kristan, W. B. & Kristan, W. B. Behavioral choice across leech species: chacun à son goût. *J. Exp. Biol.* **213**, 1356–1365 (2010).

9. Koyama, M. *et al.* A circuit motif in the zebrafish hindbrain for a two alternative behavioral choice to turn left or right. *Elife* **5**, (2016).

10. Popescu, I. R. & Frost, W. N. *Highly Dissimilar Behaviors Mediated by a Multifunctional Network in the Marine Mollusk Tritonia diomedea*. *Soc Neuroscience* (2002).

11. Soffe, S. R. Two distinct rhythmic motor patterns are driven by common premotor and motor neurons in a simple vertebrate spinal cord. *J. Neurosci.* **13**, 4456–4469 (1993).

12. Itti, L. & Koch, C. Computational modelling of visual attention. *Nat. Rev. Neurosci.* **2**, 194–203 (2001).

13. Goodhill, G. J. Contributions of theoretical modeling to the understanding of neural map development. *Neuron* **56**, 301–311 (2007).

14. Kohonen, T. Self-organized formation of topologically correct feature maps. *Biol. Cybern.* **43**, 59–69 (1982).

15. Lynch MIT, N., Musco, C. & Parter, M. Winner-Take-All Computation in Spiking Neural Networks. (2019). doi:10.48550/arxiv.1904.12591

16. Chen, Y. Mechanisms of winner-take-all and group selection in neuronal spiking networks. *Front. Comput. Neurosci.* **11**, 20 (2017).

17. Szigeti, B., Deogade, A. & Webb, B. Searching for motifs in the behaviour of larval Drosophila melanogaster and Caenorhabditis elegans reveals continuity between behavioural states. *J. R. Soc. Interface* **12**, (2015).

18. Stephens, G. J., Johnson-Kerner, B., Bialek, W. & Ryu, W. S. Dimensionality and dynamics in the behavior of C. elegans. *PLoS Comput. Biol.* **4**, (2008).

19. Gomez-Marin, A., Stephens, G. J. & Brown, A. E. X. Hierarchical compression of Caenorhabditis elegans locomotion reveals phenotypic differences in the organization of behaviour. *J. R. Soc. Interface* **13**, (2016).

20. Ahamed, T., Costa, A. C. & Stephens, G. J. Capturing the continuous complexity of behaviour in Caenorhabditis elegans. *Nat. Phys.* **17**, 275–283 (2021).

21. Lindén, H., Petersen, P. C., Vestergaard, M. & Berg, R. W. Movement is governed by rotational neural dynamics in spinal motor networks. *Nat. 2022 6107932* **610**, 526–531 (2022).

22. CROLL, N. A. Components and patterns in the behaviour of the nematode Caenorhabditis elegans. *J. Zool.* **176**, 159–176 (1975).

23. White, J., Southgate, E. & Thomson, J. The structure of the nervous system of the nematode Caenorhabditis elegans. *Trans R Soc L. B Biol …* (1986).

24. Chen, B. L., Hall, D. H. & Chklovskii, D. B. Wiring optimization can relate neuronal structure and function. *Proc. Natl. Acad. Sci. U. S. A.* **103**, 4723–4728 (2006).

25. Witvliet, D. *et al.* Connectomes across development reveal principles of brain maturation in C. elegans. (2020). doi:10.1101/2020.04.30.066209

26. Cook, S. J. *et al.* Whole-animal connectomes of both Caenorhabditis elegans sexes. *Nature* **571**, 63–71 (2019).

27. Gao, S. *et al.* Excitatory motor neurons are local oscillators for backward locomotion. *Elife* **7**, (2018).

28. Kawano, T. *et al.* An imbalancing act: Gap junctions reduce the backward motor circuit activity to bias C. elegans for forward locomotion. *Neuron* **72**, 572–586 (2011).

29. Xu, T. *et al.* Descending pathway facilitates undulatory wave propagation in Caenorhabditis elegans through gap junctions. *Proc. Natl. Acad. Sci. U. S. A.* **115**, E4493–E4502 (2018).

30. Fang-Yen, C., Alkema, M. J. & Samuel, A. D. T. Illuminating neural circuits and behaviour in *Caenorhabditis elegans* with optogenetics. *Philos. Trans. R. Soc. B Biol. Sci.* **370**, 20140212 (2015).

31. Chalfie, M. *et al.* The neural circuit for touch sensitivity in Caenorhabditis elegans. *J. Neurosci.* **5**, 956–964 (1985).

32. Gray, J. M., Hill, J. J. & Bargmann, C. I. A circuit for navigation in Caenorhabditis elegans.

Proc. Natl. Acad. Sci. U. S. A. **102**, 3184–3191 (2005).

33. Meng, J. Molecular , Cellular and Circuit Mechanisms that underlie a Two-pore Potassium C hannel ' s Regulation of Membrane Potential , Synaptic Activity and Locomotion Molecular , Cellular and Circuit Mechanisms that underlie a Two-pore Potassium C hannel ' s Reg. (University of Toronto, 2022).

34. Rodgers, J. B. & Ryu, W. S. Targeted thermal stimulation and high-content phenotyping reveal that the C. elegans escape response integrates current behavioral state and past experience. *PLoS One* **15**, (2020).

35. Mohammadi, A., Byrne Rodgers, J., Kotera, I. & Ryu, W. S. Behavioral response of Caenorhabditis elegans to localized thermal stimuli. *BMC Neurosci.* **14**, (2013).

36. Pokala, N., Liu, Q., Gordus, A. & Bargmann, C. I. Inducible and titratable silencing of Caenorhabditis elegans neurons in vivo with histamine-gated chloride channels. *Proc. Natl. Acad. Sci.* **111**, 2770–2775 (2014).

37. Goodman, M. B., Hall, D. H., Avery, L. & Lockery, S. R. Active currents regulate sensitivity and dynamic range in C. elegans Neurons. *Neuron* **20**, 763–772 (1998).

38. Goodman, M. B., Lindsay, T. H., Lockery, S. R. & Richmond, J. E. Electrophysiological Methods for C. elegans Neurobiology. *Methods Cell Biol.* **107**, 409 (2012).

39. Kato, S. *et al.* Global Brain Dynamics Embed the Motor Command Sequence of Caenorhabditis elegans. *Cell* **163**, 656–669 (2015).

40. Liu, P., Chen, B., Mailler, R. & Wang, Z. W. Antidromic-rectifying gap junctions amplify chemical transmission at functionally mixed electrical-chemical synapses. *Nat. Commun.* **8**, 1–16 (2017).

41. Xie, L. *et al.* NLF-1 Delivers a Sodium Leak Channel to Regulate Neuronal Excitability and Modulate Rhythmic Locomotion. *Neuron* **77**, 1069–1082 (2013).

42. Mellem, J., Brockie, P., Madsen, D. & Maricq, A. Action potentials contribute to neuronal signaling in C. elegans. *Nat. Neurosci.* (2008).

43. Liu, P., Chen, B. & Wang, Z.-W. SLO-2 potassium channel is an important regulator of neurotransmitter release in Caenorhabditis elegans. *Nat. Commun. 2014 51* **5**, 1–12 (2014).

44. Huang, Y. C. *et al.* Gain-of-function mutations in the UNC-2/CaV2α channel lead to excitation-dominant synaptic transmission in C. elegans. *Elife* **8**, (2019).

45. Saheki, Y. & Bargmann, C. I. Presynaptic CaV2 calcium channel traffic requires CALF-1 and the alpha(2)delta subunit UNC-36. *Nat. Neurosci.* **12**, 1257–1265 (2009).

46. Richmond, J. E. & Jorgensen, E. M. One GABA and two acetylcholine receptors function at the C. elegans neuromuscular junction. *Nat. Neurosci.* **2**, 791–798 (1999).

47. Oh, K. H., Krout, M. D., Richmond, J. E. & Kim, H. UNC-2 CaV2 Channel Localization at

Presynaptic Active Zones Depends on UNC-10/RIM and SYD-2/Liprin-α in Caenorhabditis elegans. *J. Neurosci.* **41**, 4782–4794 (2021).

48. Lesage, F. TWIK-1, a ubiquitous human weakly inward rectifying K+ channel with a novel structure. *EMBO J.* **15**, 1004–1011 (1996).

49. Cluzeaud, F. *et al.* Expression of TWIK-1, a novel weakly inward rectifying potassium channel in rat kidney. *Am. J. Physiol. - Cell Physiol.* **275**, (1998).

50. Chavez, R., Gray, A., Zhao, B. & Kindler, C. TWIK-2, a new weak inward rectifying member of the tandem pore domain potassium channel family. *J. Biol.* (1999).

51. Ben Soussia, I. *et al.* Mutation of a single residue promotes gating of vertebrate and invertebrate two-pore domain potassium channels. *Nat. Commun.* **10**, 1–13 (2019).

52. Aryal, P., Abd-Wahab, F., Bucci, G. & Sansom, M. A hydrophobic barrier deep within the inner pore of the TWIK-1 K2P potassium channel. *Nature* (2014).

53. Schmitt, C., Schultheis, C., Husson, S. & Liewald, J. Specific expression of channelrhodopsin-2 in single neurons of Caenorhabditis elegans. *PLoS One* (2012).

54. Gao, S. *et al.* The NCA sodium leak channel is required for persistent motor circuit activity that sustains locomotion. *Nat. Commun.* **6**, 6323 (2015).

55. Zheng, Y., Brockie, P. J., Mellem, J. E., Madsen, D. M. & Maricq, A. V. Neuronal control of locomotion in C. elegans is modified by a dominant mutation in the GLR-1 ionotropic glutamate receptor. *Neuron* **24**, 347–361 (1999).

56. Pirri, J. K., McPherson, A. D., Donnelly, J. L., Francis, M. M. & Alkema, M. J. A Tyramine-Gated Chloride Channel Coordinates Distinct Motor Programs of a Caenorhabditis elegans Escape Response. *Neuron* **62**, 526–538 (2009).

57. Ji, N. *et al.* Corollary discharge promotes a sustained motor state in a neural circuit for navigation. *Elife* **10**, (2021).

58. Gordus, A., Pokala, N., Levy, S., Flavell, S. W. & Bargmann, C. I. Feedback from network states generates variability in a probabilistic olfactory circuit. *Cell* **161**, 215–227 (2015).

59. Wagh, D. A. *et al.* Bruchpilot, a protein with homology to ELKS/CAST, is required for structural integrity and function of synaptic active zones in Drosophila. *Neuron* **49**, 833–844 (2006).

60. Sordillo, A. & Bargmann, C. I. Behavioral control by depolarized and hyperpolarized states of an integrating neuron. *Elife* **10**, (2021).

61. Chitturi, J. *et al.* The UBR-1 ubiquitin ligase regulates glutamate metabolism to generate coordinated motor pattern in Caenorhabditis elegans. *PLOS Genet.* **14**, e1007303 (2018).

62. Fouad, A. D. *et al.* Distributed rhythm generators underlie Caenorhabditis elegans forward locomotion. *Elife* **7**, (2018).

63. Kindt, K. S. *et al.* Dopamine Mediates Context-Dependent Modulation of Sensory Plasticity in C. elegans. *Neuron* **55**, 662–676 (2007).

64. Nguyen, J. P. *et al.* Whole-brain calcium imaging with cellular resolution in freely behaving *Caenorhabditis elegans*. *Proc. Natl. Acad. Sci.* **113**, E1074–E1081 (2016).

65. N, J. *et al.* Corollary discharge promotes a sustained motor state in a neural circuit for navigation. *Elife* **10**, (2021).

66. Ben Arous, J., Tanizawa, Y., Rabinowitch, I., Chatenay, D. & Schafer, W. R. Automated imaging of neuronal activity in freely behaving Caenorhabditis elegans. *J. Neurosci. Methods* **187**, 229–234 (2010).

67. Venkatachalam, V. *et al.* Pan-neuronal imaging in roaming Caenorhabditis elegans. *Proc. Natl. Acad. Sci. U. S. A.* **113**, E1082–E1088 (2016).

68. Bhardwaj, A., Thapliyal, S., Dahiya, Y. & Babu, K. FLP-18 functions through the G-protein-coupled receptors NPR-1 and NPR-4 to modulate reversal length in Caenorhabditis elegans. *J. Neurosci.* **38**, 4641–4654 (2018).

69. Taylor, S. R. *et al.* Molecular topography of an entire nervous system. *Cell* **184**, 4329-4347.e23 (2021).

70. Hammarlund, M., Hobert, O., Miller, D. M. & Sestan, N. The CeNGEN Project: The Complete Gene Expression Map of an Entire Nervous System. *Neuron* **99**, 430–433 (2018).

71. Hammell, C. M. & Hannon, G. J. Inducing RNAi in Caenorhabditis elegans by Injection of dsRNA. *Cold Spring Harb. Protoc.* **2016**, 80–85 (2016).

72. Ghezzi, A., Liebeskind, B. J., Thompson, A., Atkinson, N. S. & Zakon, H. H. Ancient association between cation leak channels and Mid1 proteins is conserved in fungi and animals. *Front. Mol. Neurosci.* **7**, (2014).

73. Zhao, B., Khare, P., Feldman, L. & Dent, J. A. Reversal Frequency in Caenorhabditis elegans Represents an Integrated Response to the State of the Animal and Its Environment. *J. Neurosci.* **23**, 5319 (2003).

74. Pierce-Shimomura, J. T., Morse, T. M. & Lockery, S. R. The Fundamental Role of Pirouettes in Caenorhabditis elegans Chemotaxis. *J. Neurosci.* **19**, 9557 (1999).

75. Chen, L. *et al.* Escape steering by cholecystokinin peptidergic signaling. *Cell Rep.* **38**, (2022).

76. Huang, K. M., Cosman, P. & Schafer, W. R. Machine vision based detection of omega bends and reversals in C. elegans. *J. Neurosci. Methods* **158**, 323–336 (2006).

77. Wang, Y. *et al.* Flexible motor sequence generation during stereotyped escape responses. *Elife* **9**, 1–27 (2020).

78. Witvliet, D. *et al.* Connectomes across development reveal principles of brain maturation. *Nature* **596**, 257–261 (2021).

79. Mulcahy, B. *et al.* Post-embryonic remodeling of the C. elegans motor circuit. *Curr. Biol.* **32**, 4645-4659.e3 (2022).

80. Liu, P., Chen, B., Mailler, R. & Wang, Z. W. Antidromic-rectifying gap junctions amplify chemical transmission at functionally mixed electrical-chemical synapses. *Nat. Commun.* **8**, (2017).

81. Chitturi, J. *et al.* The UBR-1 ubiquitin ligase regulates glutamate metabolism to generate coordinated motor pattern in Caenorhabditis elegans. *PLOS Genet.* **14**, e1007303 (2018).

82. Lu, Y. *et al.* Extrasynaptic signaling enables an asymmetric juvenile motor circuit to produce symmetric undulation. *Curr. Biol.* **32**, 4631-4644.e5 (2022).

83. Ashaber, M. *et al.* Anatomy and activity patterns in a multifunctional motor neuron and its surrounding circuits. *Elife* **10**, 1–30 (2021).

84. Takahashi, N., Sasaki, T., Matsumoto, W., Matsuki, N. & Ikegaya, Y. Circuit topology for synchronizing neurons in spontaneously active networks. *Proc. Natl. Acad. Sci. U. S. A.* **107**, 10244–10249 (2010).

85. Wang, Z. *et al.* The relationship of anatomical and functional connectivity to resting state connectivity in primate somatosensory cortex. *Neuron* **78**, 1116 (2013).

86. Zarin, A. A., Mark, B., Cardona, A., Litwin-Kumar, A. & Doe, C. Q. A multilayer circuit architecture for the generation of distinct locomotor behaviors in Drosophila. *Elife* **8**, (2019).

87. Atkinson, L. E. *et al.* Ascaris suum Informs Extrasynaptic Volume Transmission in Nematodes. *ACS Chem. Neurosci.* **12**, 3176–3188 (2021).

88. Sánchez, L. R. *et al.* The neuropeptidergic connectome of C. elegans. *bioRxiv* 2022.10.30.514396 (2022). doi:10.1101/2022.10.30.514396

89. Bentley, B. *et al.* The Multilayer Connectome of Caenorhabditis elegans. *PLoS Comput. Biol.* **12**, (2016).

90. Bargmann, C. I. Beyond the connectome: how neuromodulators shape neural circuits. *Bioessays* **34**, 458–465 (2012).

91. Marder, E. Neuromodulation of neuronal circuits: back to the future. *Neuron* **76**, 1–11 (2012).

92. Liu, Q., Kidd, P. B., Dobosiewicz, M. & Bargmann, C. I. C. elegans AWA Olfactory Neurons Fire Calcium-Mediated All-or-None Action Potentials. *Cell* **175**, 57-70.e17 (2018).

93. Jiang, J. *et al.* C. elegans enteric motor neurons fire synchronized action potentials underlying the defecation motor program. *Nat. Commun. 2022 131* **13**, 1–15 (2022).

94. Liu, Q., Hollopeter, G. & Jorgensen, E. M. Graded synaptic transmission at the Caenorhabditis elegans neuromuscular junction. *Proc. Natl. Acad. Sci. U. S. A.* **106**, 10823–10828 (2009).

95. Geffeney, S. L. *et al.* DEG/ENaC but not TRP channels are the major mechanoelectrical transduction channels in a C. elegans nociceptor. *Neuron* **71**, 845 (2011).

96. Lindsay, T. H., Thiele, T. R. & Lockery, S. R. Optogenetic analysis of synaptic transmission in the central nervous system of the nematode Caenorhabditis elegans. *Nat. Commun.* **2**, 306 (2011).

97. O'Hagan, R., Chalfie, M. & Goodman, M. B. The MEC-4 DEG/ENaC channel of Caenorhabditis elegans touch receptor neurons transduces mechanical signals. *Nat. Neurosci.* **8**, 43–50 (2005).

98. Ramot, D., MacInnis, B. L. & Goodman, M. B. Bidirectional temperature-sensing by a single thermosensory neuron in C. elegans. *Nat. Neurosci.* **11**, 908–915 (2008).

99. Salkoff, L., Wei, A., Baban, B., Butler, A. & Fawcett, G. Potassium channels in C. elegans. (2005).

100. El Mouridi, S. *et al.* Reliable CRISPR/Cas9 genome engineering in Caenorhabditis elegans using a single efficient sgRNA and an easily recognizable phenotype. *G3 Genes, Genomes, Genet.* **7**, 1429–1437 (2017).

101. Genome sequence of the nematode C. elegans: a platform for investigating biology. *Science* **282**, 2012–2018 (1998).

102. Salkoff, L. *et al.* Evolution tunes the excitability of individual neurons. *Neuroscience* **103**, 853–859 (2001).

103. Hoogstraaten, R. I., van Keimpema, L., Toonen, R. F. & Verhage, M. Tetanus insensitive VAMP2 differentially restores synaptic and dense core vesicle fusion in tetanus neurotoxin treated neurons. *Sci. Rep.* **10**, (2020).

104. Schiavo, G. G. *et al.* Tetanus and botulinum-B neurotoxins block neurotransmitter release by proteolytic cleavage of synaptobrevin. *Nat. 1992 3596398* **359**, 832–835 (1992).

105. Goodman, M. B. & Sengupta, P. The extraordinary AFD thermosensor of C. elegans. *Pflugers Arch.* **470**, 839 (2018).

106. Nicoletti, M. *et al.* Biophysical modeling of C. Elegans neurons: Single ion currents and whole-cell dynamics of AWCon and RMD. *PLoS One* **14**, e0218738 (2019).

107. Shindou, T. *et al.* Active propagation of dendritic electrical signals in C. elegans. *Sci. Reports 2019 91* **9**, 1–12 (2019).

108. Dobosiewicz, M., Liu, Q. & Bargmann, C. I. Reliability of an interneuron response depends on an integrated sensory state. *Elife* **8**, (2019).

109. Faumont, S., Lindsay, T. & Lockery, S. Neuronal microcircuits for decision making in C. elegans. *Curr. Opin. Neurobiol.* **22**, 580–591 (2012).

110. Armenti, S. T., Lohmer, L. L., Sherwood, D. R. & Nance, J. Repurposing an endogenous degradation system for rapid and targeted depletion of C. elegans proteins. *Dev.* **141**,

4640–4647 (2014).

111. Richmond, J. E., Davis, W. S. & Jorgensen, E. M. Unc-13 is required for synaptic vesicle fusion in C. elegans. *Nat. Neurosci.* **2**, 959–964 (1999).

112. Brockie, P. J., Mellem, J. E., Hills, T., Madsen, D. M. & Maricq, A. V. The C. elegans Glutamate Receptor Subunit NMR-1 Is Required for Slow NMDA-Activated Currents that Regulate Reversal Frequency during Locomotion. *Neuron* **31**, 617–630 (2001).

113. Qi, Y., Garren, E. & Shu, X. Photo-inducible cell ablation in Caenorhabditis elegans using the genetically encoded singlet oxygen generating protein miniSOG. *Proc.* (2012).

114. Lu, Y. *et al.* Extrasynaptic signaling enables an asymmetric juvenile motor circuit to produce symmetric undulation. *Curr. Biol.* **0**, (2022).

115. Meng, J. *et al.* Myrf ER-bound transcription factors drive C. elegans synaptic plasticity via cleavage-dependent nuclear translocation. *Dev. Cell* **41**, 180 (2017).

116. Yeh, E., Kawano, T., Weimer, R. M., Bessereau, J. L. & Zhen, M. Identification of Genes Involved in Synaptogenesis Using a Fluorescent Active Zone Marker in Caenorhabditis elegans. *J. Neurosci.* **25**, 3833 (2005).